Master's Thesis

Direct Numerical Simulations in Turbulent Boundary Layers over Rod- and Cuboid-roughened Walls: Effects of the Roughness Height

Yun Kyung Choi

Department of Mechanical Engineering

Ulsan National Institute of Science and Technology

2021

Direct Numerical Simulations in Turbulent Boundary Layers over Rod- and Cuboid-roughened Walls: Effects of the Roughness Height

Yun Kyung Choi

Department of Mechanical Engineering

Ulsan National Institute of Science and Technology

Direct Numerical Simulations in Turbulent Boundary Layers over Rod- and Cuboid-roughened Walls: Effects of the Roughness Height

A thesis submitted to
Ulsan National Institute of Science and Technology
in partial fulfillment of the
requirements for the degree of
Master of Science

Yun Kyung Choi

12/30/2020
Approved by

Advisor
Jae Hwa Lee

Direct Numerical Simulations in Turbulent Boundary Layers over Rod- and Cuboid-roughened Walls: Effects of the Roughness Height

Yun Kyung Choi

This certifies that the thesis of Yun Kyung Choi is approved.

12/30/2020

Signature

Advisor: Prof. Jae Hwa Lee

Signature

Prof. Chun Sang Yoo

Signature

Prof. Jooha Kim

Abstract

Direct numerical simulations (DNSs) of spatially developing turbulent boundary layers (TBLs) over two-dimensional (2D) rod-roughened walls and three-dimensional (3D) cuboid-roughened walls are conducted to investigate the effects of the roughness height on the flow characteristics in the outer layer. The rod elements are periodically aligned along the downstream direction with a pitch of $p_x/\theta_{in} = 12$, and the cuboid elements are periodically staggered with a pitch of $p_x/\theta_{in} = 12$ and $p_z/\theta_{in} = 3$, where p_x and p_z are correspondingly the streamwise and spanwise pitches of the roughness and θ_{in} is the momentum thickness at the inlet. The first surface roughness is placed $80\theta_{in}$ downstream from the inlet, leading to a step change from a smooth to rough surface. The rod and cuboid roughness height (k) is varied in the range of $0.1 \leq k/\theta_{in} \leq 1.8$ ($13 \leq \delta/k \leq 285$), respectively ($\delta$ is the boundary layer thickness), and the Reynolds number based on the momentum thickness (θ) is varied in the range of $Re_\theta = 300 \sim 1400$. For each case, the self-preservation form of the velocity-defect and the turbulent Reynolds stresses is achieved along the downstream direction. As the roughness height increases, the roughness function (ΔU^+) extracted from the mean velocity profiles increases, although the velocity-defect profiles for the rough-wall cases show good agreement with the profile from the smooth-wall case. The magnitude of the Reynolds stresses in the outer layer increases with an increase of k/δ. The outer layer similarity between the flows over the smooth- and rough-walls is found when $\delta/k \geq 250$ and 100 for the 2D rod and 3D cuboid, respectively. The continuous increase of the Reynolds stresses in the outer layer with an increase of k/δ is explained by a large population of very long structures over the rough-wall flows. Because the characteristic width of the structures increases continuously with an increase of k/δ for the rod and cuboid roughness, a wide width of the structures leads to frequent spanwise merging between adjacent structures. The active spanwise merging events with an increase of k/δ increase the streamwise coherence of the structures with the appearance of significant meandering.

Contents

List of Figures

List of Tables

Nomenclature

Abbreviations

1D	One-dimensional
2D	Two-dimensional
3D	Three-dimensional
DNS	Direct numerical simulation
LSM	Large-scale motion
Q2	Second-quadrant Reynolds shear stress
Q4	Fourth-quadrant Reynolds shear stress
Re	Reynolds number
TBL	Turbulent boundary layer
VLSM	Very-large-scale motion

Symbols

B	Addictive constant
B_{sand}	Addictive constant related to the sand-grain roughness type
C_f	Skin frictional drag
δ	Boundary layer thickness
δ^*	Displacement thickness
δ_o	Initial boundary layer thickness
ε	Virtual origin
f_i	Momentum forcing
k	Surface roughness height
k_s	Equivalent sand-grain roughness height
κ	Kármán constant
λ_p	Plan area density
P_d	Form drag
p_x	Roughness streamwise spacing
p_z	Roughness spanwise spacing

θ	Momentum thickness
θ_{in}	Momentum thickness at the inlet
ρ_m	Streak-merging frequency
u	Streamwise velocity component
U_∞	Free-stream velocity
v	Wall-normal velocity component
v_w	Wall-normal fluctuation on the crests of the surface roughness
w	Spanwise velocity component
x	Streamwise coordinate
x_{eq}	Streamwise locations for new equilibrium states
y	Wall-normal coordinate
z	Spanwise coordinate
$\tilde{z}_{rms}$	Root mean square of the meandering motion

1. Introduction

Townsend (1976) stated that surface roughness only exerts a direct influence on the turbulence within a few roughness heights of the wall, and the roughness effects vanish away from the wall (hereafter, Townsend's wall-similarity). Raupach et al. (1991) and Jiménez (2004) proposed that if the roughness height is relatively low compared to the boundary layer thickness with a criterion of $\delta/k \geq 40$, the interaction between the inner layer and outer layer is very weak at a high Reynolds number. In a number of studies of turbulent boundary layers in the presence of significant topographical 3D complexity of the surface roughness, the establishment of the Townsend's wall-similarity have been shown in the outer layer (Akinlade et al. 2004; Flack et al. 2005; Schultz & Flack 2007; Wu & Christensen 2007, 2010; Mejia-Alvarez et al. 2014; Squire et al. 2016, 2017). In an experimental study of TBLs with sandpaper and mesh roughness for a wide range of roughness sizes (δ/k = 16 ~ 110), Flack et al. (2007) found that the roughness effects are confined to a roughness sublayer defined as $5k$ or $3k_s$ irrespective of the height of the 3D irregular roughness.

Contrary to earlier studies of turbulent boundary layers over 3D irregular surface roughness, many numerical and experimental studies of TBLs with 2D roughness elements (i.e., rod roughness) have reported the existence of roughness effects in the outer region (Krogstad & Antonia 1999; Lee & Sung 2007; Volino et al. 2009, 2011). Lee & Sung (2007) conducted a DNS study in a TBL with 2D rod roughness (δ/k = 20) and showed that the roughness effect exists in the outer region. In addition, in an experimental study, Volino et al. (2009) showed that the rod roughness (δ/k = 32) affects the outer flow significantly due to large-scale turbulent structures induced by the surface roughness. Krogstad & Antonia (1999) conducted an experiment in a turbulent boundary layer with a circular rod-roughened wall (δ/k = 47). Despite the fact that the criterion of the roughness height for the outer layer similarity is satisfied ($\delta/k \geq 40$), they found that the surface roughness significantly affects the turbulent energy production and diffusion in the outer region. Volino et al. (2011) performed an experiment using a smaller surface roughness with δ/k = 160 compared to that in their previous study, and they also found the roughness effects on the outer flow, indicating that the criterion for outer layer similarity is not universal. Even for TBLs at a high Reynolds number, the surface roughness effect of the 2D roughness have also been found (Efros & Krogstad 2011; Krogstad & Efros 2012). Although Efros & Krogstad (2011) stated that the profiles of the Reynolds shear stress between rough and smooth-walls in the outer regions of turbulent boundary layers are similar at a high Reynolds number, the profiles in the outer layer over the rough-wall observed 10 ~ 30% larger values than that over a smooth-wall.

Even for turbulent boundary layers over 3D cube roughness, a general consensus has been pertained to the failure of the wall-similarity in the outer layer (Reynolds & Castro 2008; Lee et al. 2011, 2012; Ahn et al. 2013; Nadeem et al. 2015). In an experimental study over 3D cube-roughened wall with a

relatively large roughness height (δ/k = 28) conducted by Volino et al. (2011), they showed that the surface roughness induce large modifications in the spatial correlations of the outer turbulence. Furthermore, a numerical study by Lee et al. (2011) with 3D cube roughness elements (δ/k = 17) reported the effects of the surface roughness in the outer region based on the profiles of Reynolds stress, and they attributed these effects to the long streamwise extent of the arranged surface elements and the square planes of the roughness, which lead to strong blockage effects that create active upward motions. In a very recent experimental study by Placidi & Ganapathisubramani (2018) with LEGO^{TM} bricks of a uniform height (δ/k = 10), they also observed a lack of outer layer similarity using the Reynolds shear stress profiles. It should also be noted that the experimental studies by Cheng & Castro (2002b) and Schultz & Flack (2005) showed wall-similarity in the outer layer between rough and smooth-walls in TBLs with staggered arrays of cubes (δ/k = 12) and uniformly arrayed spheres (δ/k = 30). However, several differences were readily apparent in their Reynolds stress profiles.

In the present study, DNSs of spatially developing TBLs over 2D rod-roughened walls and 3D cuboid-roughened walls are performed to investigate the effects of the roughness height on the flow characteristics. Although wall-similarity in the outer layer has not been observed in TBLs even with a small roughness value and at a high Reynolds number, a question is raised as to whether or not a critical roughness height for the outer layer similarity exists in a flow over square-edged surface roughness elements. The rod and cuboid roughness heights are varied systematically in the range of $13 \leq \delta/k \leq 285$ at a similar Reynolds number ($Re_\theta \approx 1050$), although the width of the roughness is fixed. First, we analyze the variations of the boundary layer parameters along the downstream direction to provide a useful means of characterizing the state of the flow development of the boundary layer over rough-walls. In addition, because smooth-wall inflow data is imposed at the inlet (leading to a step change from a smooth to a rough surface $80\theta_{in}$ downstream from the inlet), the downstream positions at which the flows reach new equilibrium states over the rough-walls are estimated as a function of the roughness height. Profiles of the mean velocity, Reynolds stresses and each quadrant Reynolds shear stress over the rough-walls are then compared with those of a smooth-wall to identify the establishment of wall-similarity in the outer layer. Finally, instantaneous and statistical analyses to document the modified turbulent structures are conducted to explain the possible cause of the increase in the turbulent activity in the outer layer with an increase of the roughness height for the 2D and 3D roughness.

2. Numerical method

2.1 Numerical procedure

For an incompressible flow, the non-dimensional governing equations are

$$\frac{\partial u_i}{\partial t} + \frac{\partial u_i u_j}{\partial x_j} = -\frac{\partial p}{\partial x_i} + \frac{1}{Re_{\theta in}} \frac{\partial^2 u_i}{\partial x_j \partial x_j} + f_i, \tag{2.1}$$

$$\frac{\partial u_i}{\partial x_i} = 0, \tag{2.2}$$

where x_i represents the Cartesian coordinates and u_i denotes the corresponding velocity components. All variables are non-dimensionalized by the free-stream velocity (U_∞) and the momentum thickness at the inlet (θ_{in}), and the Reynolds number is defined as $Re_{\theta in} = U_\infty \theta_{in}/\nu$. Based on a fractional-step method with the implicit velocity-decoupling process (Kim et al. 2002), the governing equations are integrated in time. Both velocity-pressure decoupling using a block lower-upper (LU) decomposition and the additional decoupling of intermediate velocity components are achieved through approximate factorization. In this approach, the temporal terms are discretized using the second-order Crank-Nicholson method, and the coupled velocity components are resolved without iteration. All terms are resolved using a second-order central-difference scheme in space with a staggered mesh. In order to describe the surface roughness, the immersed boundary method suggested by Kim et al. (2001) is employed. The momentum forcing is explicitly computed to satisfy the no-slip condition at the roughness surface. The detailed numerical method are identical to those from our previous DNS studies in turbulent boundary layers over 2D rod and 3D cube roughness (Lee & Sung 2007; Lee et al. 2011).

2.2 Flow configuration

A schematic of the computational domain and roughness configurations are shown in figure 1(a). Here, x, y and z indicate the streamwise, wall-normal and spanwise coordinates, respectively, and u, v and w correspondingly indicate the streamwise, wall-normal and spanwise velocity components. Since the boundary layer is spatially developing in the streamwise direction, a non-periodic boundary condition should be employed in the downstream direction. Also, an auxiliary simulation for the inlet boundary condition of a TBL flow is conducted based on the method proposed by Lund et al. (1998). Although not shown here, a direct comparison of the mean velocity and root-mean-square of the velocity fluctuation profiles at $Re_\theta = 300$ show good agreement with the DNS data of Spalart (1988), where θ is the momentum thickness. In addition, since it is difficult to generate accurately turbulent inflow data

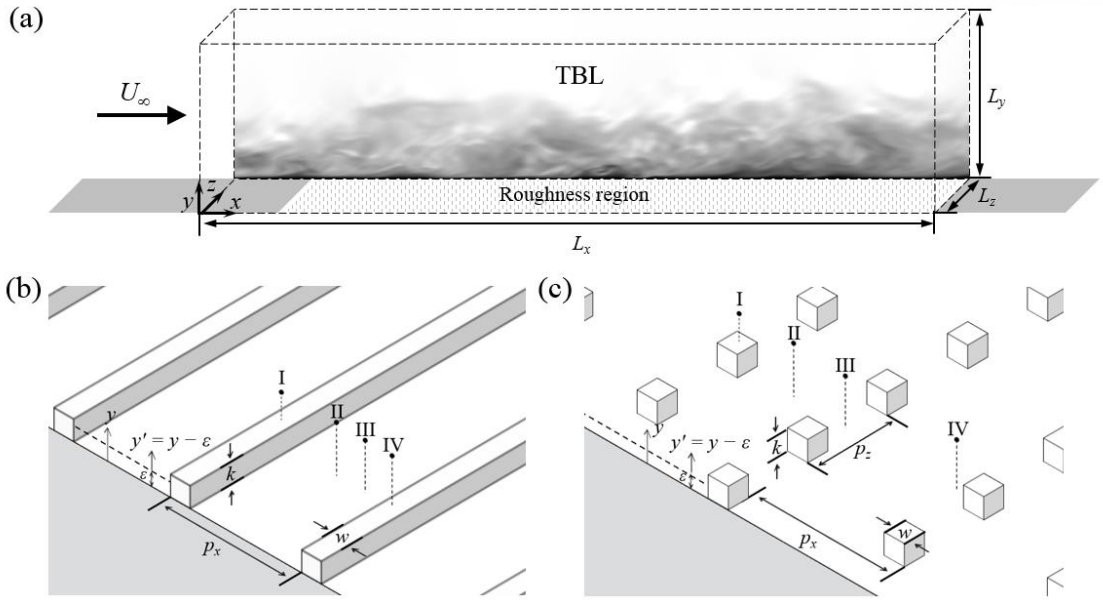

Figure 1 (a) Schematic of the computational domain and (b-c) roughness configurations for (b) a 2D rod and (c) a 3D cuboid

for a rough-wall TBL, a DNS for a TBL over a rough-wall should use a laminar Blasius velocity profile at the inlet or a smooth-wall inflow data. This leads to a significant step change in the surface condition from a smooth- to a rough-wall. Here, the first roughness element is positioned at $80\theta_{in}$ downstream from the inlet, which is defined as $x = 0$. A sufficiently long streamwise domain is used to achieve a new equilibrium state, resulting in self-preservation of a TBL within the computational domain. The computational domain sizes were confirmed to be appropriate based on the convergence of the two-point spatial correlation to zero for half of the computational domain on the horizontal plane. The no-slip boundary condition is applied at the bottom wall and the boundary conditions on the top surface of the computational domain are $u = U_\infty$ and $\partial v/\partial y = \partial w/\partial y = 0$. The spanwise boundary condition is periodic boundary condition. A non-uniform wall-normal grid distribution is employed with a hyperbolic-tangent function. In both the streamwise and spanwise direction, uniform grid distributions are used.

The roughness configurations for TBLs over the rod- and cuboid-roughened walls with a width of $w/\theta_{in} = 1.5$ are shown in figures 1(b) and (c). Because the rod elements have a maximum roughness function (ΔU^+) when the roughness height is $k/\theta_{in} = 1.5$ (Lee et al. 2012), the rod roughness are arranged periodically in the streamwise direction with a streamwise pitch of $p_x/\theta_{in} = 12$. For comparing the flow characteristics, the downstream spacing of the 3D cuboid roughness element is same with that of 2D rod roughness element. However, the cuboid roughness elements are arranged with a staggered arrangement with a spanwise pitch of $p_z/\theta_{in} = 3$ (Lee et al. 2011). Although this roughness element with the fixed p_x/θ_{in} leads to variation of the streamwise spacing with varying the roughness height, the

	k/θ_{in}	p_x/θ_{in}	L_x/θ_{in}	L_y/θ_{in}	L_z/θ_{in}	N_x, N_y, N_z	Δx^+	Δz^+	Δy_{min}^+	$\Delta t U_\infty/\theta_{in}$
smooth	-	-	1536	60	80	4097,150,257	10.2	4.2	0.14	0.1
2DK01	0.1	12	1536	60	80	4097,150,257	5.2	4.3	0.14	0.1
2DK03	0.3	12	1536	60	80	4097,150,257	5.5	4.3	0.15	0.1
2DK05	0.5	12	1536	60	80	4097,150,257	5.8	4.5	0.15	0.1
2DK07	0.7	12	768	60	80	2049,150,257	6.7	5.5	0.18	0.1
2DK11	1.1	12	768	60	80	2049,150,257	8.0	6.7	0.21	0.1
2DK15	1.5	12	768	60	80	2049,150,257	8.9	7.4	0.24	0.1
2DK18	1.8	12	768	60	80	2049,150,257	9.3	7.7	0.25	0.1
3DK01	0.1	12	1250	60	96	2500,150,513	6.9	2.6	0.14	0.1
3DK03	0.3	12	1250	60	96	2500,150,513	7.0	2.6	0.14	0.1
3DK05	0.5	12	1250	60	96	2500,150,513	7.4	2.8	0.15	0.1
3DK07	0.7	12	1250	60	96	2500,150,513	7.5	2.8	0.15	0.1
3DK11	1.1	12	768	60	96	2049,150,513	6.1	3.1	0.16	0.1
3DK15	1.5	12	768	60	96	2049,150,513	7.3	3.6	0.19	0.1
3DK18	1.8	12	768	60	96	2049,150,513	7.5	3.7	0.2	0.1

Table 1 Domain Sizes and Mesh Resolutions

roughness density (λ_p = *roughness area* / *total area*) is constant for the 2D and 3D cases, which is an important parameter that affects the flow characteristics (Leonardi & Castro 2010; Ahn et al. 2013). In Table1, the domain sizes and mesh resolutions are summarized. In the present study, the simulation names in the first column denote the dimension of the roughness type and second column indicate the roughness height; for example, 2DK15 indicates the case of 2D rod-roughened wall with a surface roughness height of $1.5\theta_{in}$. The wall-normal distance from the virtual origin is defined as $y' = y - \varepsilon$. For scrutiny of the turbulent statistics and structure, four downstream locations (I-IV) within a one pitch are indicated. In case of the 2D rod roughness, I is located at the center of the roughness crest and II is located at the center of two adjacent rods in the streamwise direction. III is located at three quarters of the roughness pitch and IV is located in front of the leading edge of the roughness. For the 3D cuboid case, the streamwise locations I, II and IV are identical to those in the 2D rod case. III is defined between

two adjacent cuboids in the spanwise direction.

In the present study, time- and spatially averaging in the spanwise direction are employed to obtain converged turbulent statistics for the 2D rough- and smooth-walls. The turbulent statistic for the 3D rough-walls are obtained by temporally and phase-averaging in the spanwise direction. A bracket $\langle\cdot\rangle$ and capital letters (e.g., U) indicate temporally- and spatially-averaged statistics. The velocity fluctuations (e.g., u') are defined as $u' = u - U$. The superscript + denotes normalization of the mean quantity by the local friction velocity (U_τ) or viscous length scale (ν/U_τ).

3. Turbulent statistics

3.1 Scaling parameter

In order to deliver similarity of the mean profiles or comparing flow generated under different conditions, the appropriate scaling parameter should be considered. Figures 2(a-c) shows the variations of the skin frictional drag ($1/2C_f$), form drag (P_d) and friction velocity (U_τ) along the downstream direction. For simplicity, the data with the roughness heights of k/θ_{in} = 0.1, 0.3, 0.7 and 1.5 are only depicted. The scaling parameters are spatially averaged over one pitch for each roughness cases (i.e., p_x/θ_{in} = 12 for a rod roughness, p_x/θ_{in} = 12 and p_z/θ_{in} = 3 for a cuboid roughness). The skin frictional drag and form drag are directly computed by the wall pressure and wall shear stress. The magnitudes of the skin frictional drag decrease with increasing the roughness height for the 2D rod and 3D cuboid rough-

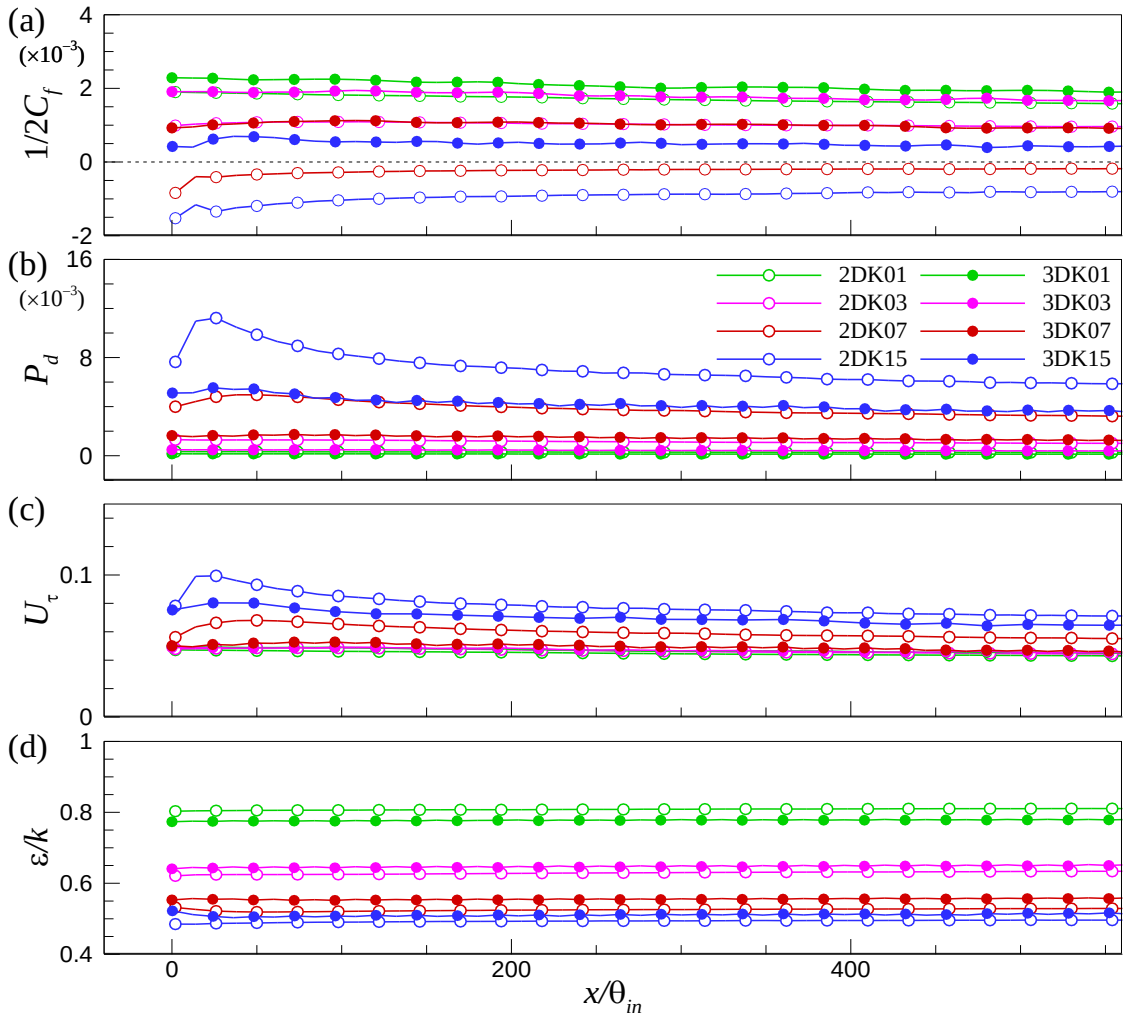

Figure 2 Variations of the spatially averaged (a) skin frictional drag ($1/2C_f$), (b) form drag (P_d), (c) frictional velocity (U_τ) and (d) virtual origin (ε/k) along the downstream direction

walls. In particular, in cases of large 2D rod roughness (i.e., 2DK07 and 2DK15), the skin frictional drag is negative over the rough-walls due to the presence of a large recirculation region with two vortices within the cavity (Lee & Sung 2007). However, in case of the large 3D cuboid roughness, the skin frictional drag is still positive due to the presences of the recirculation within the cavity is confined to the front of the cuboid and the flow within the cavity moves parallel to the streamwise direction (Coceal et al. 2007; Lee et al. 2011). In figure 2(b), as the magnitude of k/θ_{in} increases, the value of P_d increases continuously. Since the blockage effects are relatively weak for cuboids roughness compared to that for rod roughness, the magnitude of the form drag for the 3D cuboid roughness is lower than that for the 2D rod roughness. The frictional velocity in figure 2(c) is directly computed from the total drag of the form drag and skin frictional drag. The frictional velocity for TBLs over the rough-walls appears to converge to a nearly constant at approximately after $x/\theta_{in} > 300$. Furthermore, the frictional velocity for a relatively large 3D roughness cases (i.e., $k/\theta_{in} \geq 0.7$) is much smaller than those for the corresponding 2D rod roughness cases because of a large contribution of the form drag.

The variations of the virtual origin normalized by the roughness height (ε/k) over TBLs along the downstream direction are shown figure 2(d). The virtual origin is computed by defining M as the moment due to the forces in the streamwise direction, $M = \sum_{y=0}^{k} \left(P_d y \right) + C_f k$, resulting in $\varepsilon = M / (C_f + P_d)$ as reported by Jackson (1981). The virtual origin approaches almost half of the roughness height for a large roughness (i.e., $k/\theta_{in} \geq 0.7$). However, as the roughness height decreases, the magnitude of ε/k increases to approximately 0.6 for $k/\theta_{in} = 0.3$ and 0.8 for $k/\theta_{in} = 0.1$. Since the contribution from the skin friction drag becomes dominant for small roughness height cases with negligible influence of the form drag, the magnitudes of ε/k appear to converge unity with a decrease of roughness height according to the definition above. These results are similar to a previous DNS study in turbulent channel flows with 2D rod roughness with the variation of the ratio of the cavity pitch to the roughness height (p_x/k) ranging $1.33 \leq p_x/k \leq 20$ (Leonardi et al. 2003). They observed that that when the magnitude of p_x/k is less than $p_x/k = 3$, the skin-frictional drag-dominated *d*-type behavior is exhibited because shedding vortices behind the roughness does not sweep into the flow between the roughness elements. Similarly, the vortex shedding from the elements becomes progressively smaller as the roughness height decreases, and the flow is undisturbed by the roughness elements, resulting in a reduction of the form drag.

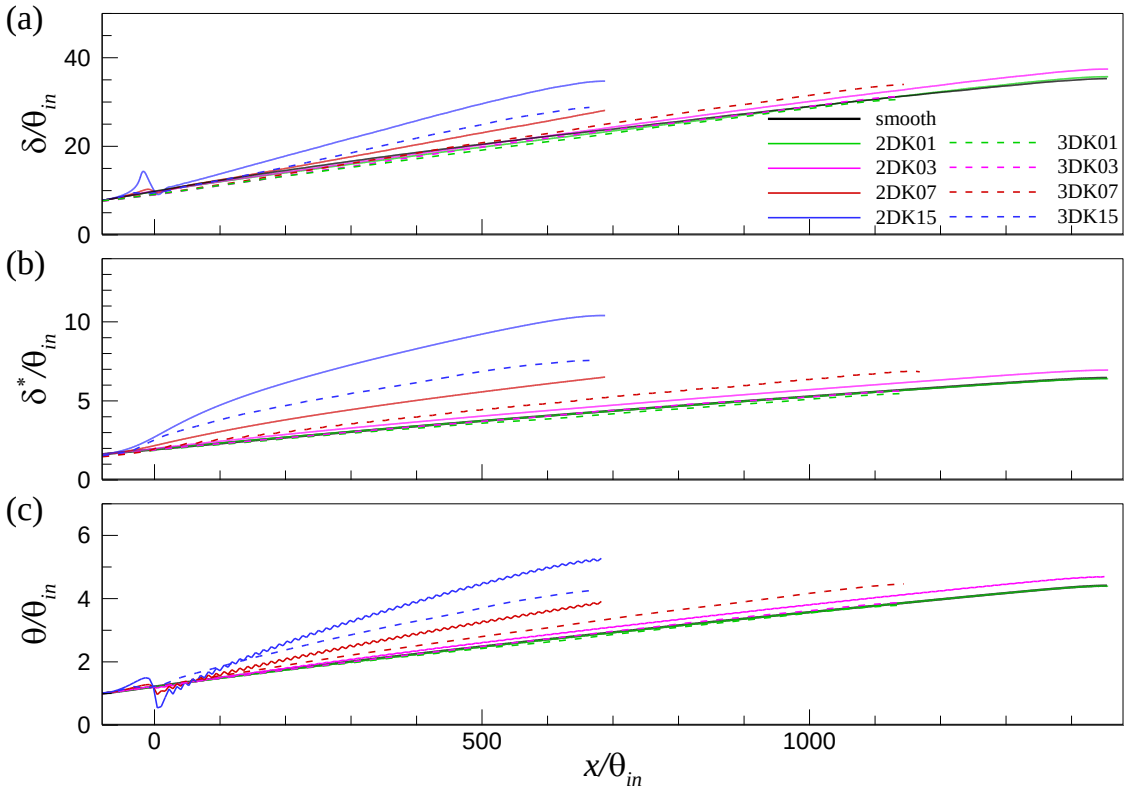

Figure 3 Variations of (a) the boundary layer thickness (δ/θ_{in}), (b) the displacement thickness (δ^*/θ_{in}) and (c) momentum thickness (θ/θ_{in}) along the downstream direction

The variations of the boundary layer thickness (δ), the displacement thickness (δ*) and the momentum thickness (θ) along the streamwise direction is shown in figure 3. The growth rates of the integral quantities for the rough-walls are larger than those for the smooth-wall case. As the value of k/θ_{in} decreases, the growth rates decrease. Since the growth rates is large for the large roughness, the Reynolds number increases significantly within a short streamwise distance. In order to match the Reynolds number, the simulations for the smooth- and rough-walls with small roughness heights are performed using relatively long streamwise computational domains (see Table 1).The integral quantities in the rough-walls become similar to those in the smooth wall as the roughness height decreases. The rapid growth rates for the 2D rough-wall TBL relative to those in the 3D rough-wall TBL indicate the strong impact on TBLs over the 2D rod rough-walls all values of k/θ_{in}.

3.2 Self-preservation of rough-wall flows

Because it is difficult to generate realistic turbulent inflow data for a spatially developing TBL with surface roughness elements, an abrupt surface step change at a streamwise location from a smooth- to a rough-wall is necessary. There is a transitional region after the step change from a smooth- to a rough-wall, which employs the new boundary condition at the bottom wall with roughness elements, after

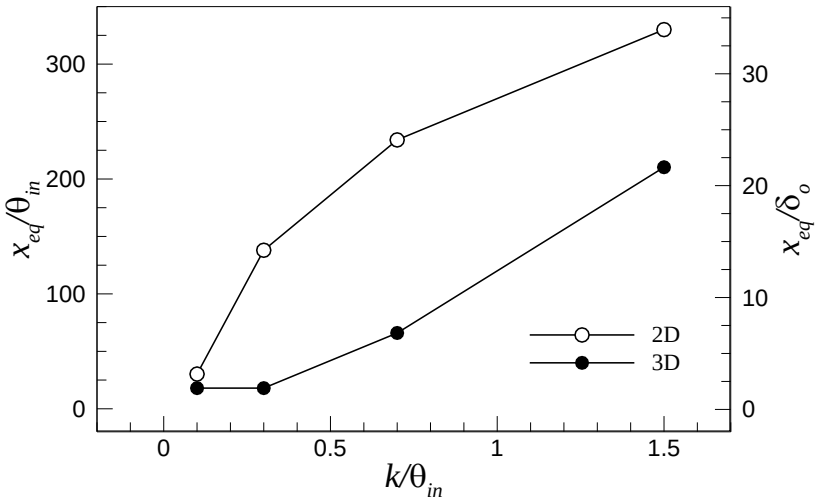

Figure 4 Variations of downstream distances (x_{eq}) from the step change required to achieve new equilibrium states, normalized by the inlet momentum thickness (θ_{in}) and initial boundary layer thickness at $x = 0$ (δ_o)

which the flow achieves a new equilibrium state through a long downstream domain. Then a self-preservation form is established. Smalley et al. (2001) suggested conditions for self-preservation in a rough-wall TBL; the magnitude of the virtual origin and the friction velocity should be constant along the downstream streamwise and the boundary layer thickness should grow linearly along the streamwise direction. In addition, Antonia & Luxton (1971) proposed that the mean velocity profiles and the intensities of turbulent intensities should approach the self-preserving form along the streamwise direction to establish an equilibrium state in turbulent boundary layer. Based on these criteria from the earlier studies (Antonia & Luxton 1971; Smalley et al. 2001), we examine the streamwise locations for new equilibrium states (x_{eq}/θ_{in}) when the magnitude of k/θ_{in} in the 2D and 3D rough-wall TBLs varies.

The variations of the streamwise locations for the new equilibrium states (x_{eq}) with respect to the roughness height are shown in figure 4. For simplicity, the detailed process is omitted because all procedures used to extract the streamwise locations for x_{eq} are identical to as those in previous studies (Lee & Sung 2007; Lee et al. 2011). In figure 4, as roughness height increases for the 2D rod and 3D cuboid rough-walls, new fully developed profiles for the rough-wall are established at a location just past about $2 \sim 33\delta_o$ downstream, where δ_o is inlet boundary layer thickness at a point for the step change. This indicates strong dependence of the magnitude of x_{eq} on the roughness geometry and height; the streamwise distance required for new fully developed profiles for the rough-walls increases with the increase of the impact of the surface roughness. Because a large roughness induce a significant impact on TBL due to the strong perturbation in the initial stage of the step change, a long streamwise distance is necessary to overcome the strong disturbance generated from the surface roughness. Given that the

disturbance due to presence of 2D rod roughness becomes significant near the step change compared to that for the 3D cuboid roughness, a sudden increase of the rate of x_{eq} is observed for small k/θ_{in} range for the 2D rod. On the other hand, the increase in the value of x_{eq} for a large roughness ($k/\theta_{in} \geq 0.7$) is similar for the 2D and 3D roughness cases. Contrary to our finding ($x_{eq} = 33\delta_o$) of 2DK15, the earlier studies by Antonia & Luxton (1971) and Krogstad & Nickels (2006) showed that the equilibrium state arises at $x_{eq} = 20\delta_o$ to adapt to the new wall condition in TBLs over an instance of 2D rod roughness ($p_x/k = 8$). Because the roughness elements in their study was imposed on the bottom wall (i.e., cavity-type roughness), the disturbance of the roughness elements on the TBL near the step change was relatively weak. The results for the 2D and 3D rough-walls in figure 4 are similar with a previous experimental study by Cheng & Castro (2002a), who showed the roughness effect using cube-type roughness staggered with a fixed plan area density ($\lambda_p = 0.25$). When a surface condition in a turbulent boundary layer was shifted from a smoother to a rougher surface with the corresponding roughness lengths y_{01} and y_{02}, they reported that the value of x_{eq} became proportional to the ratio of y_{02}/y_{01}.

3.3 Roughness sublayer

The presence of surface roughness induces substantial changes in the flow field not only in the near-wall regions but also in certain layers above the crest of the roughness. This near-wall region is known as the roughness sublayer. In a DNS study by Bhaganagar et al. (2004), they defined the extent of the roughness sublayer as the point from the wall where the turbulence statistics in a TBL become spatially homogeneous. On the other hand, Jiménez (2004) estimated the depth of the roughness sublayer based on the wall-similarity between smooth- and rough-walls in the outer layer, and the height of the roughness sublayer is about $5k$ when $\delta/k \geq 40$. Schultz & Flack (2005) proposed that the equivalent sand-grain roughness height, k_s is a better representative length scale than the roughness height (k) for defining the extent of the roughness sublayer because k_s is a general measure of the effects of the roughness on the mean flow. Flack et al. (2007) found that the distance from the wall directly affected by the roughness is limited to a region of $y < 5k$ or $y < 3k_s$ from the wall for the irregular 3D surface roughness regardless of the roughness height.

According to the definition of the roughness sublayer by Bhaganagar et al. (2004), the variation of the mean velocity and the Reynolds stress profiles along the streamwise direction for 2DK01, 2DK07 and 2DK15 is plotted in figure 5. The data are obtained after the equilibrium state is established at a similar Reynolds number ($Re_\theta \approx 1050$) and approximate streamwise locations for 2DK01, 2DK03, 2DK07 and 2DK15 are $x/\theta_{in} = 966$, 870 and 342 (i.e., 80th rod, 47th rod and 28th rod). To avoid crowding of the data in figure 5, $\langle u'u' \rangle^+$ and $\langle w'w' \rangle^+$ are shifted upwards two units and one unit respectively. Furthermore, three vertical dashed lines for $y' = 3k_s$, $5k_s$ and $5k$ are depicted to determine the wall-normal extent of the roughness sublayer. For 2DK01 in figures 5(a) and (b), the deviation of the profiles

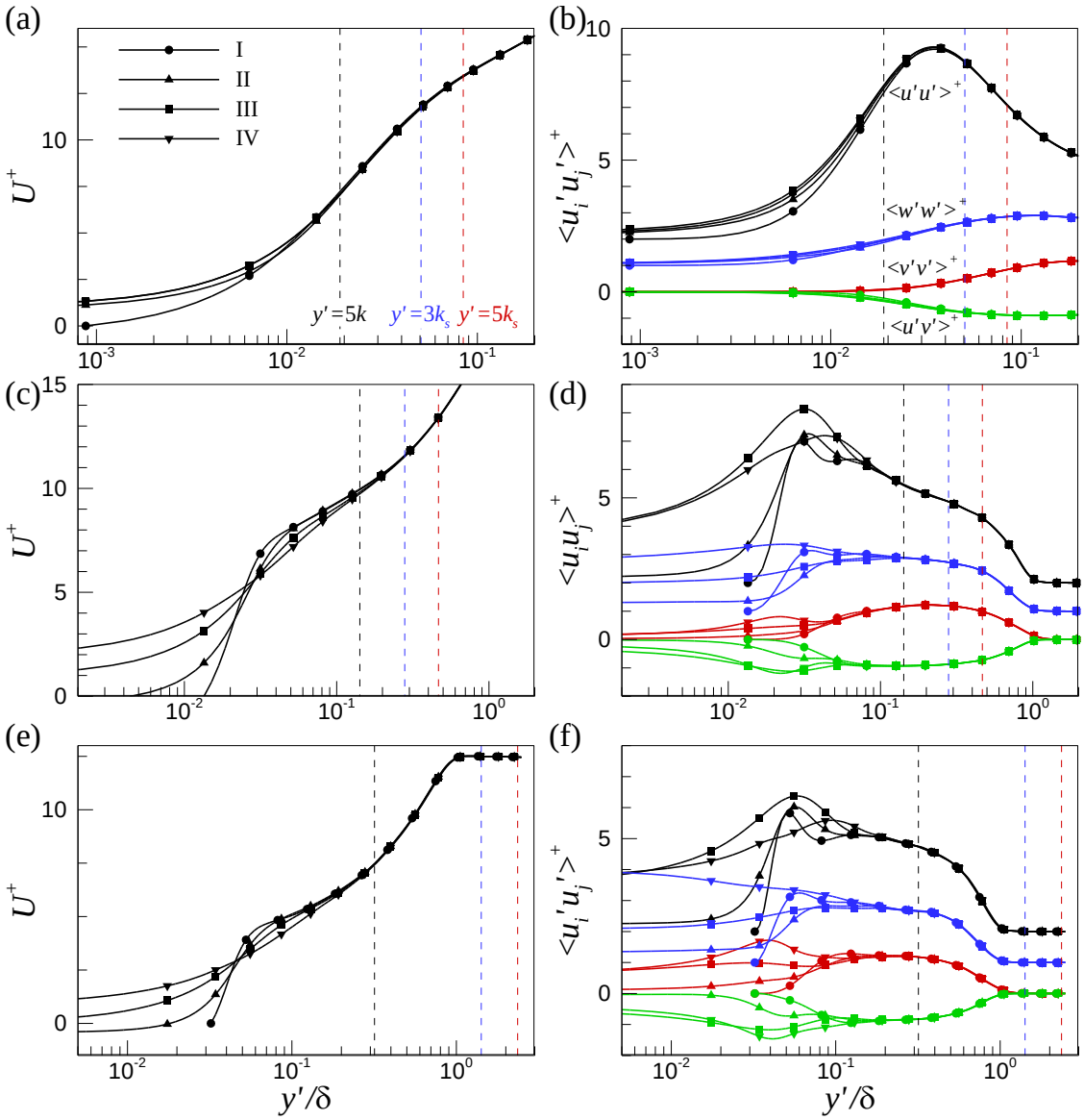

Figure 5 The mean velocity and Reynolds stresses at locations I-IV, normalized by the local friction velocity: black, $\langle u'u'\rangle^+$; blue, $\langle v'v'\rangle^+$; red, $\langle w'w'\rangle^+$; green, $\langle u'v'\rangle^+$. $\langle u'u'\rangle^+$ and $\langle w'w'\rangle^+$ are shifted upwards two and one units to avoid crowding respectively. Black dashed line, $y' = 5k$; blue dashed line, $y' = 3k_s$; red dashed line, $y' = 5k_s$. (a,b) 2DK01, (c,d) 2DK07 and (e,f) 2DK15

along the downstream direction becomes negligible for $y' \geq 3k_s$ ($y'/\delta \geq 0.05$) (see blue dashed lines). Similarly, the depth of the roughness height for 2DK07 is estimated as $y' = 3k_s$ ($y'/\delta = 0.28$) in figures. 5(c) and (d) since the roughness effect persists over $y' = 5k$ ($y/\delta = 0.14$). For 2DK15 in figures 5(e) and (f), the entire boundary layer is identified as the roughness sublayer (blue and red lines) when $y' = 3k_s$ ($3k_s/\delta = 1.42$) or $5k_s$ ($5k_s/\delta = 2.36$) is used to define the depth of the roughness sublayer (Volino et al. 2009). As a result, the height of the roughness sublayer for 2DK15 is estimated as $y' = 5k$ ($y'/\delta = 0.32$),

	x/θ_{in}	Re_θ	U_τ/U_∞	δ/θ_{in}	ΔU^+	k^+	k_s/k	δ/k	ε/k
smooth	980	1050	0.0451	28.5	-	-	-	-	-
2DK01	966	1050	0.0461	28.3	0.1	1.4	4.3	257	0.74
2DK03	870	1053	0.0485	27.6	1.2	4.4	2.5	89	0.62
2DK07	570	1050	0.0593	24.9	5.3	12.5	3.3	35	0.53
2DK15	342	1062	0.0796	23.6	9.9	35.8	6.6	16	0.49
3DK01	1014	1044	0.0458	28.5	0.1	1.4	3.7	285	0.78
3DK03	990	1045	0.0466	28.5	0.6	4.2	1.9	96	0.65
3DK07	870	1056	0.0499	27.2	2.4	10.5	2.1	39	0.56
3DK15	558	1048	0.0646	26.3	7.2	29.1	3.0	16	0.51

Table 2 Flow Parameters in Equilibrium States over Rough-walls

as highlighted by black dashed lines. These observations indicate that the outer layer similarity for the rod-roughness is achieved when the wall-normal limit of the roughness sublayer is defined as $y' = 5k$ and $y' = 3k_s$ for the large ($k/\theta_{in} > 0.7$) and small ($k/\theta_{in} \leq 0.7$) roughness respectively. Using irregular 3D surface roughness (i.e., sandpaper and mesh), Flack et al. (2007) also reported the depth of the roughness sublayer from the wall as $y' = 5k$ or $y' = 3k_s$. However, because the ratio of k_s/k was not significant (less than 3) in their study, the depth of the layer directly modified by the roughness ($y' = 5k$ or $y' = 3k_s$) is almost equivalent irrespective of the roughness geometry and size. Although not shown here, similar features are found for the 3D cuboid roughness elements.

3.4 Outer layer similarity between rough and smooth-walls

Based on the first- and second-order turbulent statistics, the wall-similarity in the outer layer between smooth- and rough-walls is examined in this section. The data for the smooth- and rough-walls are obtained at a similar Reynolds number (i.e., $Re_\theta \approx 1050$) where the self-preservation is established over the TBLs. In addition, it is known that the turbulent statistics within one roughness pitch is spatially homogeneous above the roughness sublayer (Bhaganagar et al. 2004). Thus, only the statistics at

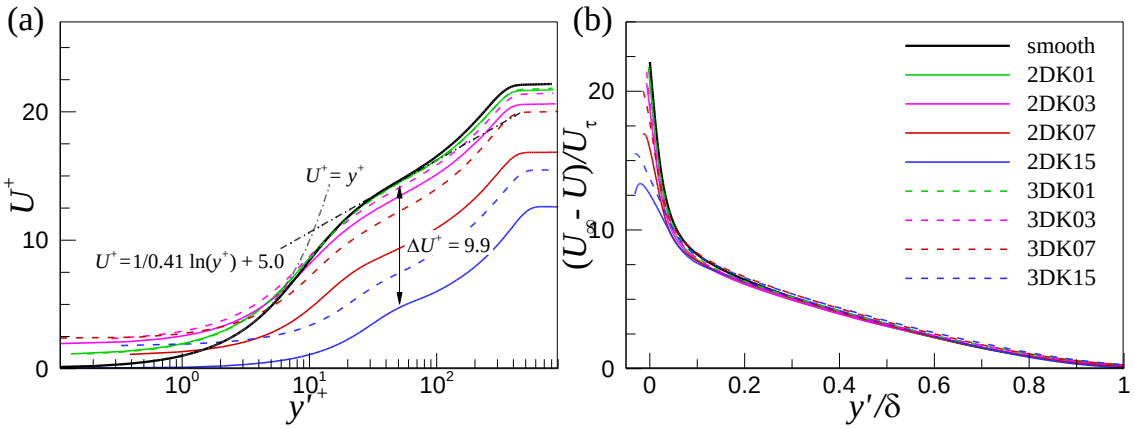

Figure 6 (a) Mean streamwise velocity profiles and (b) mean velocity-defect profiles normalized by the local friction velocity in TBLs over the smooth and rough-walls. In (a), the roughness function ΔU^+ is depicted for 2DK15 as a representative case.

location II are examined to highlight the effect of the roughness height on the turbulent boundary layer. The flow parameters for the flows over the 2D rod and 3D cuboid roughness elements with a similar Reynolds number, including roughness height, boundary thickness, the friction velocity and others, are summarized in Table 2.

3.4.1 Mean velocity profiles

For a turbulent boundary layer with surface roughness, the mean streamwise velocity can be described as follows:

$$U^+ = \frac{1}{\kappa} \ln \frac{y' U_\tau}{\nu} + B - \Delta U^+ \tag{3.1}$$

where κ is the Kármán constant (κ = 0.41), B is an additive constant (B = 5.0) and ΔU^+ is the roughness function. Figure 6 shows the mean streamwise velocity profiles for the flows over the smooth-wall and the 2D and 3D rough-walls. In case of the smooth-wall, the mean streamwise velocity profiles in the viscous sublayer and the overlap region are well expressed by $U^+ = y^+$ and $U^+ = \frac{1}{\kappa} \ln \frac{y U_\tau}{\nu} + B$ respectively. In the logarithmic region, a downshift of the mean streamwise velocity is evident when surface roughness is positioned under the bottom wall. The roughness function, ΔU^+, can express the extents of these downshifts (e.g., ΔU^+ = 9.9 for 2DK15 in figure 6a). The exact values for the flows over the 2D and 3D rough-walls are summarized in Table 2. Since the drag increment for the rough-wall can be characterized by the values of ΔU^+, the roughness function can represents the 'strength' of

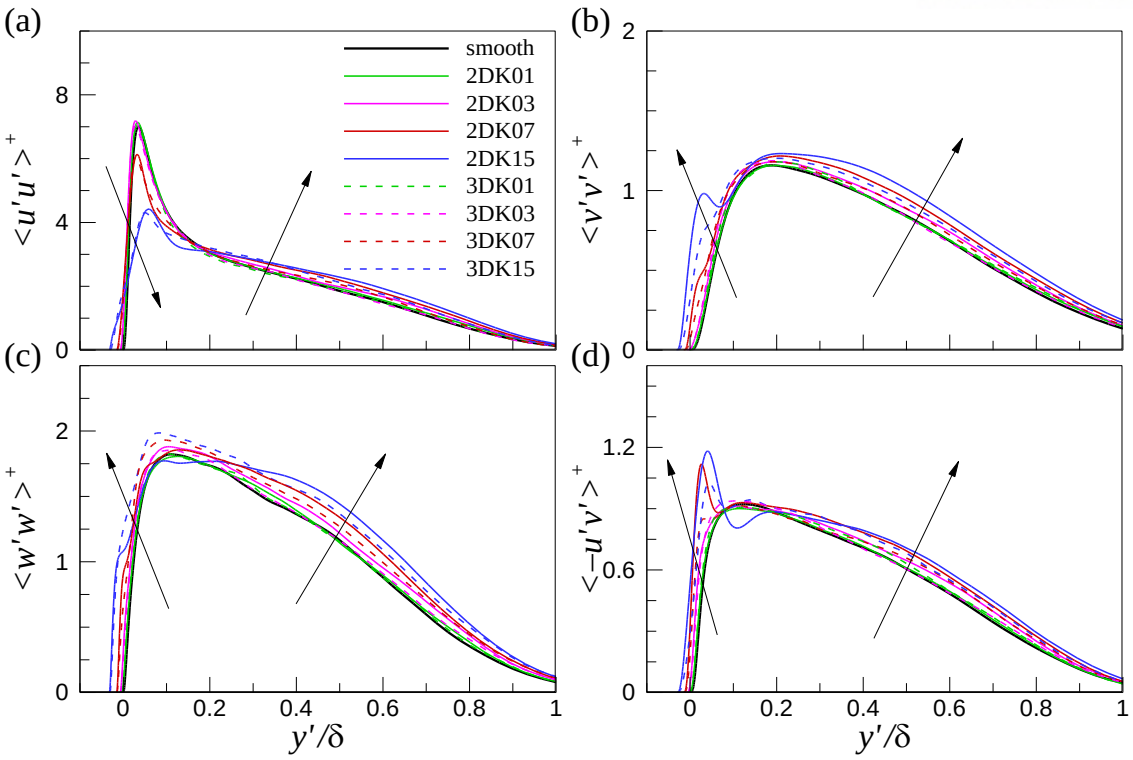

Figure 7 Profiles of the Reynolds stresses normalized by the local friction velocity in the outer coordinates in TBLs over smooth and rough-walls

surface roughness. It is obvious that the values of roughness function are very small for the small roughness heights (i.e., 2DK01, 3DK01, 3DK03). The value of the roughness function increases continuously with increasing of the roughness height. Because the total drag of the 3D cuboid is relatively weak (figure 2c) compare to the 2D rough-walls, and the value of the roughness function of the 3D roughness is small even the roughness height is identical. The profiles of the velocity-defect form for the 2D and 3D rough-walls in figure 6(b) show a good agreement in the outer region with that for the smooth-wall, indicating that the outer mean flow is less sensitive.

3.4.2 Reynolds stress profiles

In figure 7, the profiles of the Reynolds stresses in the outer coordinates are show for the flows over the 2D rod and 3D cuboid rough-walls. The inner peaks of the streamwise Reynold stress $<u'u'>^+$ downshift as k/θ_{in} increases for the 2D rod and 3D cuboid rough-walls. This is because the streamwise vortical structures in the near-wall layer (e.g., quasi-streamwise vortices and low-speed streaks) are attenuated by the presence of the surface roughness. On the other hand, as k/θ_{in} increases for the flows over the 2D and 3D rough-walls, the near-wall peaks of the wall-normal components in the roughness sublayer (at y'/δ= 0.15 ~ 0.20) increase. This can be caused by the flow collision by the presence of the surface roughness, leading to the turbulent isotropy from the streamwise direction to the wall-normal direction.

The values of $<u'u'>^+$ and $<v'v'>^+$ in the near-wall region for the 3D rough-walls are smaller than those for the 2D rough-walls. However, the magnitude of $<w'w'>^+$ in the near-wall later is greater for the 3D rough-walls than for the 2D rough-walls, especially for 3DK15 (blue dashed line). This results suggests that although the energy redistribution over the 3D cuboid-roughened wall is not active due to the relatively weak blockage effect, the flow running away from the middle of the two adjacent roughness elements with the spanwise-offset characteristic interacts with the cuboids and upstream flow, leading to the presence of strong spanwise fluctuations. With an increasing value of k/θ_{in} (≥ 0.7) (corresponding to $k/\delta \geq 0.03$), a abrupt decrease of the inner peak of spanwise Reynolds stress $<w'w'>^+$ is observed in case of the 2D roughness. This is because the velocity component in the streamwise direction tends to redistribute to the y-direction rather than z-direction. In addition, as the roughness height increases, new peaks for $<v'v'>^+$, $<w'w'>^+$ and $<u'v'>^+$ are observed along the lip of the cavity ($y'^+ = 30 \sim 40$ or $y'/\delta = 0.05 \sim 0.1$) (especially for 2DK15). These new peaks is expected because the local decrease of the turbulent activity slightly above the cavity lip in the roughness valley (location II) highlights the near-wall strength of the Reynolds stresses compared to that near the trailing and leading edges (Lee et al. 2009).

Clearly, as k/θ_{in} increases over the 2D rod and 3D cuboid rough-wall flows, the values of the Reynolds stress increases in the outer region. If we assume that wall-similarity in the outer region is achieved when the deviation of the Reynolds stresses between the rough- and smooth-walls is less than 5%, the wall-similarity in the outer layer in the outer region between the flows over rough- and smooth-walls is established with the sufficiently small roughness. In particular, the deviation for 2DK01, 3DK01 and 3DK03 compared to the data obtained from the profiles of smooth-wall is approximately 2% at $y'/\delta = 0.5$, where the maximum deviation in the Reynolds stresses between the rough- and smooth-walls is found. On the other hand, the difference is estimated to be approximately 6 ~ 22% for the other rough-wall cases. The continuous increment of the Reynolds stresses in the outer region with increasing of the value of k/θ_{in} is consistent with a previous finding by Ligrani & Moffat (1986) in turbulent boundary layers with uniform sphere roughness ranging of $21 \leq k^+ \leq 63$.

3.4.3 Quadrant analysis

In order to examine the modification of turbulent motions regarding on the contributions of turbulent events to the total production (or destruction) of the Reynolds shear stress, a quadrant analysis is conducted (Lu & Willmarth 1973). The quadrant analysis allows the classification of flow events into four quadrants of planes composed of u' and v'. In figure 8, the profiles of each quadrant Reynolds shear stress in the outer coordinates for smooth- and rough-walls are shown. Since the second-quadrant (Q2) and fourth-quadrant (Q4) stresses make dominant contribution to the generation of $<u'v'>$, only second- and fourth-quadrant Reynolds shear stress profiles are plotted in figure 8. In case of the smooth-wall,

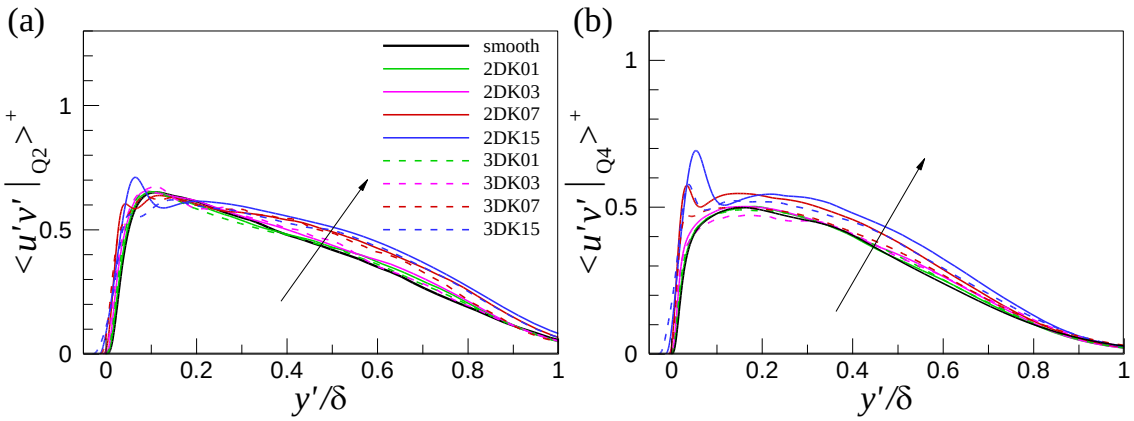

Figure 8 Profiles of the Reynolds shear stresses from each quadrant normalized by the local friction velocity in TBLs over rough-walls

the motion of ejection mostly contribute to the Reynolds shear stress in the outer region compared to the motion of sweep, because the spanwise-oriented vortical motions are dominant in this region. In case of the rough-wall in a TBL with 2D rod and 3D cube roughness, as k/θ_{in} increases, the Q2 ejection and Q4 sweep events enhance in the outer region. The deviation in the Q2 ejection and Q4 sweep events between the rough- and smooth-walls is less than about 1 ~ 4% for 2DK01, 3DK01 and 3DK03 but not for the remaining cases (15 ~ 23%), consistent with results from the profiles of the Reynolds stress (figure 7).

It is known that the effects of the roughness in the outer region for the flows over 2D rod and 3D cube roughness is directly associated with the spacing of the surface roughness (p_x/θ_{in} or p_z/θ_{in}) (Lee et al. 2012; Ahn et al. 2013; Nadeem et al. 2015). In a DNS study by Lee et al. (2012), they explored the influence of the streamwise spacing (p_x/θ_{in}) for the flows over the rod and cube roughness elements both in the inner and outer layer. As the streamwise spacing varied ranging of p_x/k = 2 ~ 10, the value of the Reynolds stresses in the outer region have was proportional to p_x/k. In comparison, for the 2D rod and 3D cube roughened wall, the wall-friction parameters (e.g., P_d, U_τ and ΔU^+) yielded local maxima at specific values of p_x/k = 8 and 4, respectively. It is worthy to note that the spanwise pitch for the cube roughness elements was fixed in their study (p_z/k = 2). In addition, based on systematic variations of cube roughness (p_x/k = 3) with respect to the spanwise pitch in the range of p_z/k = 2 ~ 6, a subsequent study of Ahn et al. (2013) showed that although the maximum contributions to the roughness function and form drag appear at a specific roughness density (i.e., $\lambda_p \simeq 0.12$), the value of the Reynolds stress in the outer layer is proportional to the magnitude of p_x/k for the 2D rod and 3D cube rough-wall cases. Contrary to earlier studies in which the tendency of the wall-friction parameters varies from the Reynolds stress tendency in the outer region, the variations of the Reynolds stress and the wall-friction parameters in the outer region are similar with increasing the roughness height in the present study.

Therefore, the influence of the 2D and 3D roughness elements on the inner and outer layer is significantly determined by the height of the surface roughness, and the outer-similarity is achieved for $k/\theta_{in} \leq 0.1$ ($\delta/k \geq 250$) for the two-dimensional rod roughness and for $k/\theta_{in} \leq 0.3$ ($\delta/k \geq 100$) for the three-dimensional cuboid roughness. However, it is worthy to note that since the *Re* employed here is low, further experiments or simulations that explore the effect of the roughness height on turbulent boundary layers over various roughness configuration at high *Re* are required to clarify the wall-similarity in the outer region more clearly in the future study.

3.4.4 Parameterization of ΔU^+ for the prediction of outer layer similarity

In general, the surface roughness appears in various sizes and shapes. It is useful to determine a parameter that can represent the 'strength' of roughness. Here, the magnitude of ΔU^+ has been adopted as a possible candidate in order to measure the momentum deficit induced by surface roughness in the outer layer (Nikuradse 1933; Schlichting 1937; Flack & Schultz 2014). Given that the roughness height plays an important role in the overlap region as opposed to the viscous length scale, the mean velocity profile in the overlap region for a rough-wall flow can be written as

$$U^+ = \frac{1}{\kappa} \ln \frac{y'}{k} + B_r, \tag{3.2}$$

where B_r is an additive constant for the case of a rough wall. Eqs. (3.1) and (3.2) are rearranged to derive the roughness function in the overlap region,

$$\Delta U^+ = \frac{1}{\kappa} \ln k^+ + B - B_r. \tag{3.3}$$

Various data (including our data) obtained from the geometrically different rough-walls are plotted together in figure 9(a) to reveal the relationship between the roughness function and the roughness height (k^+) (Nikuradse 1933; Schultz & Flack 2005; Flack et al. 2007; Schultz & Flack 2009). Although the variation of ΔU^+ with respect to k^+ shows a log-linear profile for a high roughness height for each case, the overall data are scattered with some offsets in the plot.

As a remedy, the equivalent sand-grain roughness height (k_s) can be utilized to yield the best collapse of the roughness function regardless of the roughness configuration (Nikuradse 1933; Schlichting 1937; Jiménez 2004). To realize this, Eq. (3.3) is reformulated by the equivalent sand-grain roughness height,

$$\Delta U^+ = \frac{1}{\kappa} \ln k_s^+ + B - B_{sand}, \tag{3.4}$$

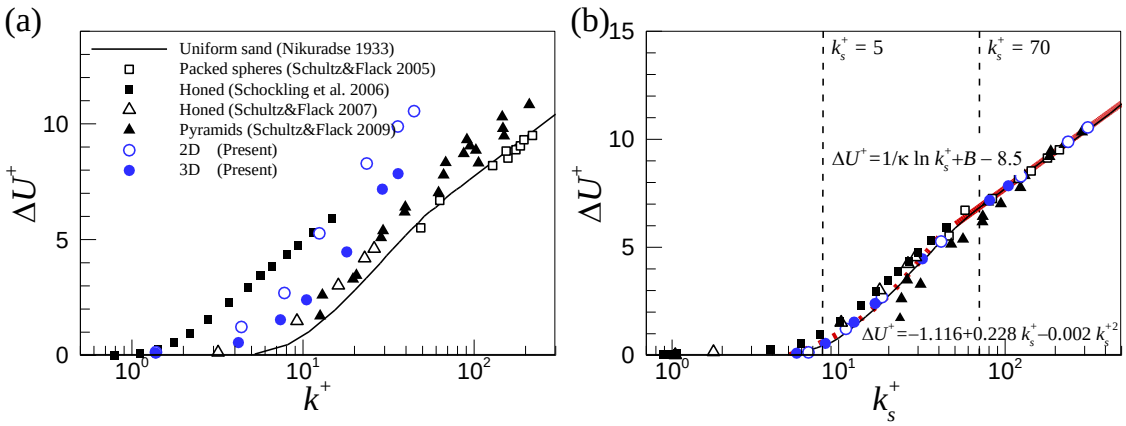

Figure 9 Variation of the roughness function (ΔU^+) as a function of (a) k^+ and (b) k_s^+. Red lines in (b) show line fits to the data: red solid line ($\Delta U^+ = 1/\kappa \ln k_s^+ + B - 8.5$), fully-rough; red dashed line ($\Delta U^+ = -1.116 + 0.228k_s^+ - 0.002k_s^{+2}$), hydraulically smooth to transitionally rough. Furthermore, vertical dashed lines indicate boundaries between hydraulic-smooth and transitional-rough (i.e., $k_s^+ = 5$) and between transitional-rough and fully rough cases (i.e., $k_s^+ = 70$).

where B_{sand} is an additive constant related to the sand-grain roughness type. Using Eqs. (3.3) and (3.4), the ratio between the equivalent sand-grain roughness height and roughness height is determined by

$$k_s^+ / k^+ = \exp[\kappa(B_{sand} - B_r)]. \tag{3.5}$$

To obtain an independent value of k_s with which to plot figure 9(b), B_{sand} and B_r in Eq. (3.5) should be computed. In figure 10(a), the values of B_{sand} as a function of k_s^+ measured by Nikuradse (1933) are denoted by the black circles. The experimental data vary monotonically with an increase of k_s^+. Based on the curve of B_{sand}, Nikuradse (1933) classified roughness types into three regimes (black vertical dashed lines): hydraulically smooth, transitionally rough and fully rough. When k_s^+ is very small ($k_s^+ \leq 5$, *hydraulically smooth*), all perturbations generated by the roughness elements are completely attenuated by the fluid viscosity, and the roughness elements have a negligible effect on the viscous sublayer. As a result, B_{sand} grows almost linearly with respect to k_s^+. When k_s^+ is large ($k_s^+ \geq 70$, *fully rough*), the viscous drag is negligible compared to the form drag induced by the roughness element, and B_{sand} has a constant value along with k_s^+. In this regime, the skin friction coefficient is independent of the Reynolds number. The intermediate regime where the near-wall characteristics are influenced by both the pressure and viscous drag are referred to as *transitionally rough* ($5 < k_s^+ < 70$).

In figure 10(b), the estimated values of B_r using Eq. (3.3) are plotted for geometrically different rough surfaces (including our data). The values of B_r clearly show strong dependence on the roughness geometry, especially for a large k^+, and this effect leads to the scattering profiles for the various rough-wall data shown in figure 9(a). The data for the 2D rod and 3D cuboid cases vary monotonically with

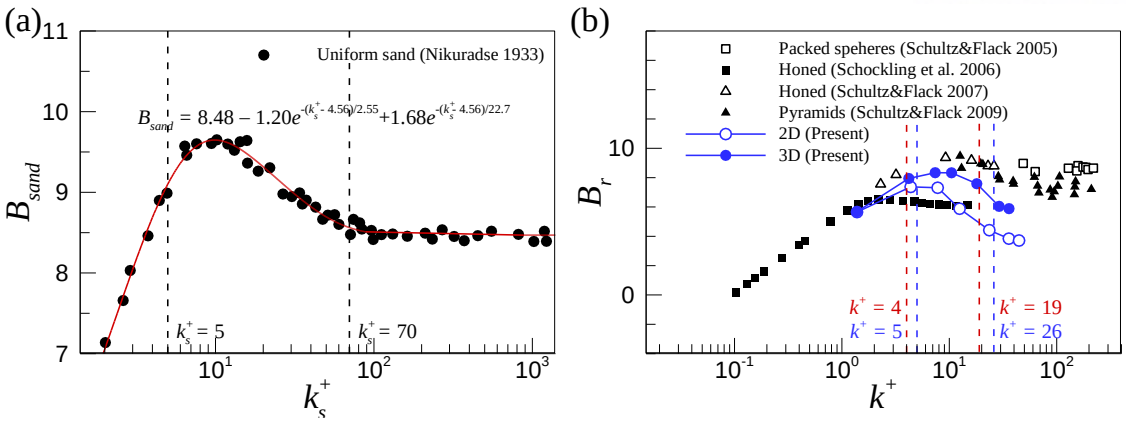

Figure 10 Variations of (a) B_{sand} as a function of k_s^+ and (b) B_r as a function of k^+. In (a), vertical dashed lines indicate boundaries between hydraulic-smooth and transitional-rough and between transitional-rough and fully rough cases (Nikuradse 1933), and the red solid line shows the fit to the data by minimizing the mean square error. In (b), vertical dashed lines indicate the boundaries between hydraulic-smooth and transitional-rough and between transitional-rough and fully rough cases for 2D (red) rod and 3D (blue) cuboid roughness.

an increase of k^+. For a small k^+ (i.e., hydraulically smooth), the values of B_r increase almost linearly in the range of $k^+ \leq 4$ for a 2D rough-wall and $k^+ \leq 5$ for a 3D rough-wall. After inflectional behavior, the values of B_r in the range of $k^+ \geq 19$ and $k^+ \geq 26$ (i.e., fully rough) approach constant values of 4.0 and 5.7 for the 2D rod and 3D cuboid roughness, respectively, similar to the behavior of B_{sand} in figure 10(a) The boundaries of the roughness type are plotted in figure 10(b) with red and blue dashed lines for the rod and cuboid cases, respectively. Because the critical values of k^+ for the flow regime for the 2D and 3D roughness are determined by Nikuradse's criterion (i.e., $k_s^+ = 5$ and 70), there is a discrepancy according to the roughness configuration in the present study. The boundaries observed in figure 10(b) are inconsistent with those in an earlier experimental result by Bandyopadhyay (1987), who found that a TBL flow with $k^+ > 10$ over a rod-roughened wall is assumed to be a fully rough regime. Because the roughness configuration in their study used values of $p_x/k = 3.8$ and $w/k = 0.75$, the critical value of the roughness height for the fully rough regime was decreased by the relatively strong impact of the surface geometry.

Using the data of B_r and B_{sand} in figure 10, the equivalent sand-grain roughness height (k_s^+) is computed based on Eq. (3.5). Because the values of B_r and B_{sand} are characterized by constant values for the fully rough regime in figure 10, the equivalent sand-grain roughness height can be determined by a linear relationship based on Eq. (3.5), which corresponds to $k_s^+ = 6.3 \times k^+$ for the 2D rod and $k_s^+ = 3.0 \times k^+$ for the 3D cuboid. This magnitude for the 2D rough wall is similar to that in a previous experimental study in a turbulent boundary layer over 2D rod rough-wall by Krogstad & Antonia (1999), which used $k_s/k \simeq 6$. The almost doubled value of the constant for the 2D rough-wall compared to that

for the 3D rough-wall suggests that the 2D rod roughness has twice as strong an impact for the fully rough regime compared to the 3D cuboid roughness under the present roughness configuration.

After the magnitude of k_s^+ is determined for all flow types using Eq. (3.5), the roughness function as a function of k_s^+ is estimated, as shown in figure 9(b). The present data are in good agreement with Nikuradse's fit (black sold line) from a hydraulically smooth regime to a fully rough regime. The roughness function for $k_s^+ \geq 70$ (fully rough regime) clearly shows a log-linear relationship (red solid line, $\Delta U^+ = \frac{1}{\kappa} \ln k_s^+ + B - 8.5$), consistent with previous studies for various roughness types in a fully rough regime, e.g., sandpaper, packed spheres and uniform sand (Colebrook 1939; Ligrani & Moffat 1986; Schultz & Flack 2007). As the value of k_s^+ decreases ($k_s^+ < 70$), the roughness function for the rod and cuboid roughness is well expressed by $\Delta U^+ = -1.116 + 0.228 k_s^+ - 0.002 k_s^{+2}$ (red dashed line) without a distinction between hydraulic-smooth and transitional-rough regimes. Based on the boundaries for the flow regimes in figure 9(b), it is clear that wall-similarity in the outer layer for the 2D and 3D roughness is established near the lower limit of the transitionally rough regime (i.e., $k_s^+ \simeq 11$), and the corresponding range of ΔU^+ for the establishment of wall-similarity is $\Delta U^+ < 1.2$. Although the transitionally rough regime in figure 9(b) is consistent with a previous experimental observation (i.e., $5 < k_s^+ < 70$) by Nikuradse (1933) for a TBL with sand-grain roughness, Shockling et al. (2006) and Schultz & Flack (2007) presented that a transitionally rough regime spans $2.5 < k_s^+ < 30$ for a honed pipe type of roughness. The discrepancy of the flow boundaries is most likely due to the inconsistent methods used to determine the equivalent sand-grain roughness height. Shockling et al. (2006) reported that the equivalent sand-grain roughness height of the surface element is simply determined by $k_s \simeq 3k$. However, as described in figure 10(b), the values of B_r in the range of $k^+ < 3$ considered in their study should be characterized by an inflectional profile due to exponential behavior (Eq. 3.5).

Another method to evaluate the magnitude of ΔU^+ is found through the wall-normal fluctuation on the crests of the surface roughness (v_w^+) suggested by Orlandi et al. (2006) and Orlandi & Leonardi (2008). They reported that the value of ΔU^+ is linked to the value of v_w^+ for the various configuration of surface roughness (e.g., triangular, circular, square rod roughness and aligned, wedged and staggered cuboid roughness). In order to provide a new universal parameterization through the magnitude of v_w^+ with respect to the roughness height, the variation of v_w^+ with respective to k_s^+ is plotted in figure 11(a). As k_s^+ increases, the value of v_w^+ increases for the flows over 2D and 3D roughness elements. Particularly, due to the small ratio of k_s/k for the 3D cuboid roughness, the value of v_w^+ increases rapidly for the 3D rough-wall in the transitional-rough regime compare to that for the 2D rough-wall. However, in the fully rough regime, the growth rate of v_w^+ as a function of k_s^+ is very similar regardless of the dimension of the surface roughness. As depicted by the red dashed line in figure 11(a), it is found that

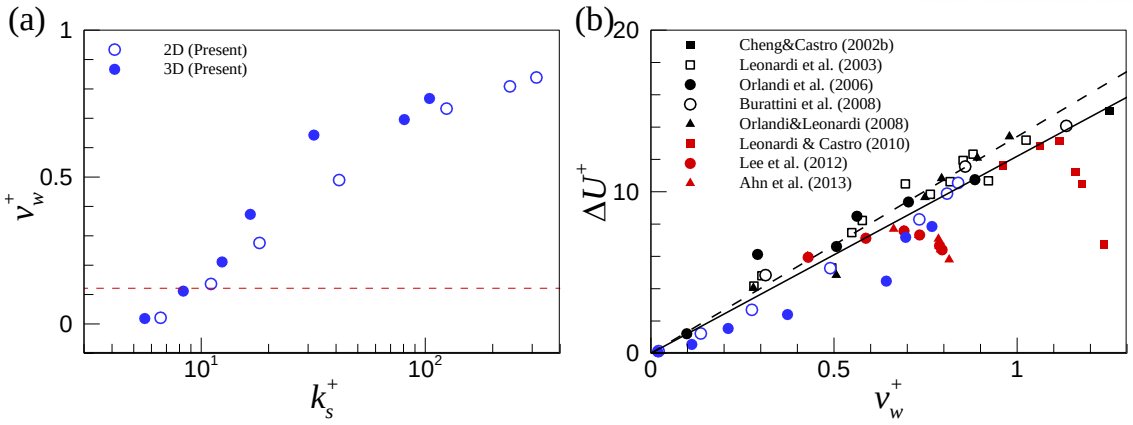

Figure 11 Variations of (a) the wall-normal fluctuations at the plane of the roughness crests (v_w^+) as a function of k_s^+ and (b) the roughness function (ΔU^+) as a function of v_w^+. In (a), the red horizontal dashed line indicates a critical value for the establishment of wall-similarity in the outer layer. In (b), solid line, $\Delta U^+ = B/\kappa\, v_w^+$ (B = 5.0); dashed line, $\Delta U^+ = B/\kappa\, v_w^+$ (B = 5.5). Open and closed symbols indicate the 2D and 3D surface roughness, respectively.

the effects of the roughness exist in the outer region, while in the range of $v_w^+ < 0.11$, weak interaction between the inner and outer layers is found for 2D and 3D rough-walls. The strong correlation between the Reynolds stress and the v_w^+ in the outer region with a critical value indicates that the value of v_w^+ is a proper parameter for the estimation of wall-similarity in the outer layer for flow over square-edged rough-walls. However, due to the fact that a critical value is sensitive to the roughness configuration (e.g., p_x and p_z), a more thorough analysis is necessary to estimate a universal parameterization of v_w^+ with respective of the roughness configuration.

The variation of roughness function with respective of v_w^+ with various data obtained from geometrically different rough-walls is shown in figure 11(b). Orlandi et al. (2006) and Orlandi & Leonardi (2008) suggested the linkage of the roughness function and v_w^+ as $\Delta U^+ = B/\kappa\, v_w^+$, where B = 5.5 for turbulent channel flows for various configurations of 2D and 3D surface roughness. Similar to earlier observations depicted by the black symbols, as the roughness heights increase, our results for 2D rod rough-walls show that there is a linear relationship between ΔU^+ and v_w^+ (blue open circle). Since the magnitude of ΔU^+ for the establishment of wall-similarity in the outer layer is estimated to $\Delta U^+ < 1.2$ in figure 9, the corresponding value of v_w^+ for wall-similarity based on the linear relationship is $v_w^+ \simeq 0.1$ when B = 5.0, consistent with that obtained in figure 11(a). In comparison, considerable deviations in the data for the flows over the 3D cuboid rough-walls in figure 11(b) are observed throughout the entire range (blue closed circles). Although ΔU^+ and v_w^+ increases monotonically with an increase of roughness height for the 3D rough-wall (figure 9b and 11a), the growth rate of ΔU^+ is relatively small than the growth rate of v_w^+ due to less flow disturbance induced by the 3D roughness

elements. For example, although the magnitudes of v_w^+ for the 2D rod and 3D cuboid roughness are similar for each ratio of the roughness height, when k/θ_{in} increases from k/θ_{in} = 0.3 to k/θ_{in} = 1.5, the increase of ΔU^+ is 523% for the 2D rough-wall and 493% for the 3D rough-walls (figure 11a). Lee et al. (2012) (red closed circle), Leonardi & Castro (2010) (red closed rectangle) and Ahn et al. (2013) (red closed triangle) reported similar failures for the prediction of ΔU^+ with respect to v_w^+ in turbulent boundary layers over 3D surface roughness distributions. Although the v_w^+ decreased monotonically with increasing the plan area density of the surface roughness, the magnitude of ΔU^+ had a local maxima at $\lambda_p \simeq 0.12$ in their studies. However, it is noteworthy that for the three-dimensional roughness arrays employed in earlier finding by Cheng & Castro (2002b) and Orlandi & Leonardi (2008), the data did not significantly deviate from the linear relationship because they only considered high roughness density beyond a critical value of λ_p for a peak.

4. Coherent structures

Previous observations of the turbulent wall-bounded flows (e.g., channel, pipe and boundary layer) for the smooth-walls observed the organization of coherent structures, and these vortical structures tend to align coherently to form low- and high-streaky patterns, corresponding to large-scale motions (LSMs) with streamwise lengths of $1 \sim 3\delta$ and very-large-scale motions (VLSMs) with streamwise extents greater than 3δ (Head & Bandyopadhyay 1981; Adrian et al. 2000; Christensen & Adrian 2001; Ganapathisubramani et al. 2003; Hutchins & Marusic 2007; Lee & Sung 2011; Baltzer et al. 2013; Lee et al. 2019). In an experimental study, Ganapathisubramani et al. (2003) found that large-scale u'-streaky structures contribute to a large fraction of the total mean Reynolds shear stress, although they occupy less than 4.5% of the total area. Furthermore, in a turbulent pipe flow study, Wu et al. (2012) found that VLSMs with wavelengths greater than $3R$ contribute more than 30% of the Reynolds shear stress and more than 40% of the streamwise turbulent energy. In this section, in order to determine the origin of the active turbulent motions in the outer layer with increasing the roughness height. The modifications of the turbulent coherent structures in the outer layer are examined.

Since the vortical structures in raw flow fields appears in very complex topology with multi-scales and various strength, it is useful to extract the characteristic lines pertaining to these coherent structures. The extraction is helpful to identify the spatial organizations of coherent structures. In the present study, the characteristic lines of u'-structures are extracted based on the streak detection algorithm by Lee et al. (2014). The algorithm is briefly explained below.

Step 1: The instantaneous flow field is filtered using a two-dimensional Gaussian filter on the cross-stream plane to attenuate the small-scale features of u'. In order to divide a negative structure from adjacent negative structures, the half-width of the spanwise two-point spatial correlation coefficient ($R_{u'u'}$) with a contour level of $R_{u'u'} = 0.15$ is used to the estimation of the standard deviation of the Gaussian filter along the wall-normal direction.

Step 2: In order to separate large-scale structures from small-scale structures, a long-wavelength-pass filter is employed to the Gaussian-filtered flow fields with a cutoff wavelength of $\lambda_z/\delta = 0.5$ (Basley et al. 2019).

Step 3: A characteristic line is determined from each negative u'-structures in the filtered flow fields using local minima of $\partial u'/\partial z = 0$ and $u' < -u_{th}$, where u_{th} is the threshold level of detection. The magnitude of u_{th} to identify the low-momentum regions is carefully chosen to be 10% of the free-stream velocity.

The instantaneous flow fields of the δ-scaled u'-structures on the xz-plane at $y'/\delta = 0.2$ is shown in figure 12. The data is chosen within the equilibrium region at approximately $Re_\theta = 1050$. Only case of

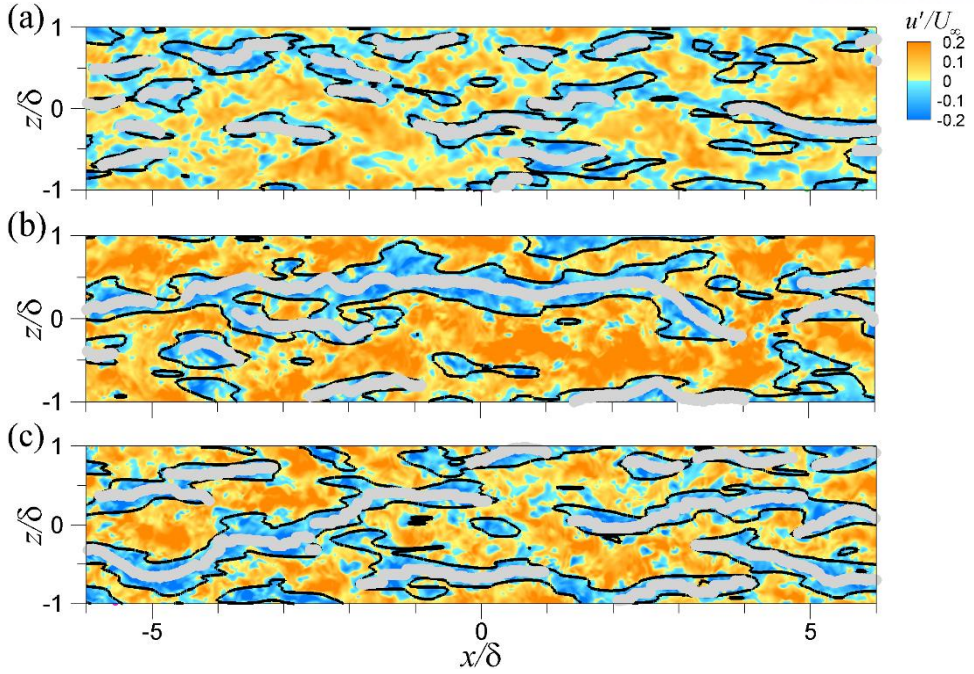

Figure 12 Instantaneous flow fields of the δ-scaled u'-structures (u'/U_∞) on the xz-plane at y'/δ = 0.2: (a) smooth, (b) 2DK15 and (c) 3DK15. Grey lines indicate negative characteristic lines. Black lines indicate filtered u'/U_∞ with magnitudes of –0.05.

k/θ_{in} = 1.5 is plotted as a representative case here for the 2D rod and 3D cuboid roughness. Based on the streak identification algorithm, the characteristic lines of the u'-structures as depicted by grey lines are superimposed onto the instantaneous flow fields. In case of the smooth-wall in figure 12(a), the negative u'-streaks are aligned along the downstream direction, and these structures are flanked with the positive u'-streaks (yellow contour) in the spanwise direction. The streamwise length of the negative u'-structure is about 1 ~ 2δ with characteristic spanwise widths close to 0.2 ~ 0.3δ, forming large-scale structures. These spatial features of the negative u'-structures for the smooth-wall are highly consistent with earlier studies of such TBLs for the smooth-wall flows (Tomkins & Adrian 2003; Wu & Christensen 2010). For the flows over the 2D rod and 3D cuboid rough-walls in figures 12(b) and (c), the negative u'-streaks appears similar patterns to the patterns of the u'-streaks over the smooth-wall TBL. In contrary, the streamwise extent of the negative structures appears to be much longer with a wider spanwise width than that of the smooth-wall flow. In particular, a very-large-scale streaky pattern is shown with a characteristic length of approximately ~9δ and a width of approximately 0.3 ~ 0.5δ for the 2D rod rough-wall. Despite of the fact that very long patterns are also found for the smooth-wall flow, the population of these streaky patterns is relatively low than the case of rough-walls. These results suggest that a large population of long streak patterns with high energy leads the increase of the Reynolds stresses in the outer layer, consistent with earlier studies based on energy spectrum (Nadeem et al. 2015; Lee et al. 2016). The spatial features of the u'-streaks over the rough-wall flow resemble

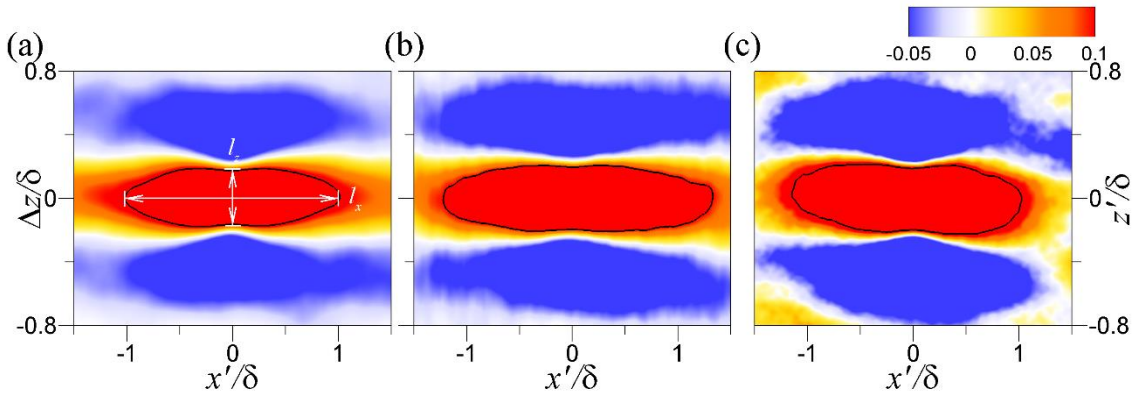

Figure 13 Streamwise two-point correlation $R_{u'u'}$ on the *xz*-plane at y'_{ref}/δ =0.2: (a) smooth, (b) 2DK15 and (c) 3DK15. The solid line indicates a low contour level of $R_{u'u'}$ = 0.1. The axis is not scaled. In (c), the *y*-axis is depicted on the right.

VLSM in smooth-wall turbulent pipe flows (Baltzer et al. 2013; Lee et al. 2019) and the 'superstructures' observed in a smooth-wall TBL flow (Hutchins & Marusic 2007). In spite of the fact that the streamwise coherence of the negative *u*′-streaks increases in the TBLs over the 2D and 3D rough-walls in figure 12 (Volino et al. 2011; Lee et al. 2016), it has often been reported a reduction of the streamwise length scale of the coherent structures in the TBLs over the irregular 3D roughness, e.g., an actual turbine blade and mesh-type roughness, because flow structures are broken to streamwise scales approximate the roughness size (Volino et al. 2007; Wu & Christensen 2010).

If the spatial features are commonly found in the instantaneous flow fields, it must leave an imprint on the statistics sense. In the present study, the two-point correlation of the streamwise velocity fluctuations ($R_{u'u'}$) is considered. The two-point spatial correlation coefficients of the streamwise fluctuating velocity in turbulent boundary layers over 2D and 3D rough-walls are defined as follows:

$$R_{u'u'}(x', y', \Delta z; x_{ref}, y_{ref}) = \frac{\left\langle u'(x_{ref}, y_{ref}, z)u'(x', y', z+\Delta z)\right\rangle}{\sigma_{u'}(x_{ref}, y_{ref})\sigma_{u'}(x', y')} \quad \text{for 2D rod,} \qquad (4.1)$$

$$R_{u'u'}(x', y', z'; x_{ref}, y_{ref}, z_{ref}) = \frac{\left\langle u'(x_{ref}, y_{ref}, z_{ref})u'(x', y', z')\right\rangle}{\sigma_{u'}(x_{ref}, y_{ref}, z_{ref})\sigma_{u'}(x', y', z')}, \quad \text{for 3D cuboid,} \qquad (4.2)$$

where subscript '*ref*' indicate the reference location for each direction, and $\sigma_{u'}$ is the root mean square of streamwise velocity fluctuation. The definition of the two-point spatial correlation coefficient is identical to that in Eq. (4.1) in case of flow over the smooth-wall. The contours of the correlations of the streamwise velocity fluctuation on the *xz*-plane is shown in figure 13. The wall-normal location of y'_{ref}/δ = 0.2 is chosen as the reference location for 2D rod and 3D cuboid roughness, and the streamwise

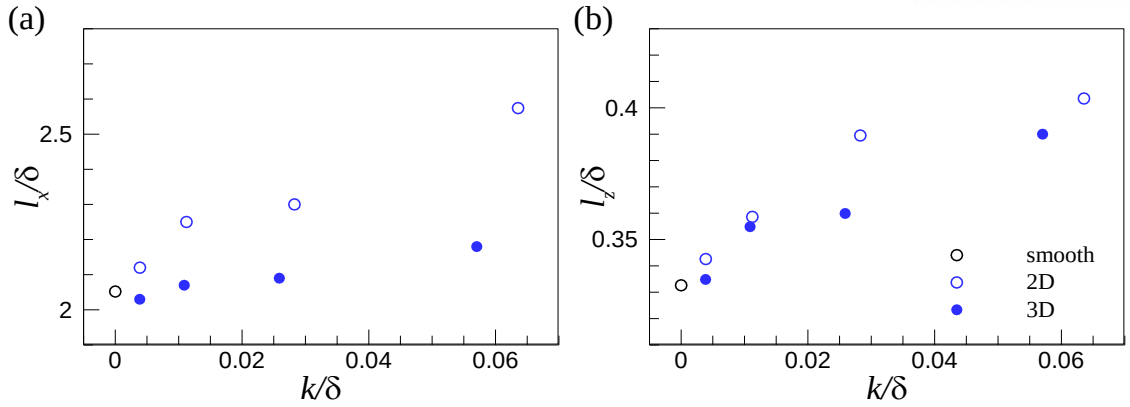

Figure 14 Variations of the characteristic (a) streamwise length scale (l_x) and (b) spanwise length scale (l_z) extracted from the correlation contour ($R_{u'u'}$ = 0.1) with an increase of the roughness height

reference location is the center of the roughness valley at approximately Re_θ = 1050. In case of the flows over 3D cuboid roughness, the spanwise reference location is the center between two adjacent roughness elements in the streamwise direction (location II). In order to show the predominance of structures with large-scales towards one or the other direction, the symmetric condition in the spanwise direction because of the spanwise homogeneous feature is not employed in the contours for the smooth and rod-roughened walls. Since the overall correlation pattern with low- or intermediate-level contours (for example, $R_{u'u'}$ = 0.1 or 0.3) can be interpreted as imprints of long u'-streaky patterns, a correlation level of 0.1 with a streamwise length of approximately 4-5δ (black solid line) is highlighted. In figures 12(b) and (c), it is clear that the streamwise extents of the contours ($R_{u'u'}$ = 0.1) for the 2D and 3D roughness cases becomes longer 28% and 9% than that for the smooth-wall. In addition, the spanwise length scale of the contours $R_{u'u'}$ = 0.1 is wider by approximately 21% and 18% compared to that for the smooth-wall. Figure 14 shows quantitative variation of the streamwise and spanwise length scales of the correlations as a function of k/δ for the 2D and 3D rough walls, aside from the correlation patterns for 2DK15 in figure 13. Based on the correlation of $R_{u'u'} > 0.1$, the streamwise and spanwise length scales are estimated here, and the reference location is identical to that in figure 13. As the roughness height increase for the 2D and 3D rough-walls, the streamwise and spanwise coherence of the u'-structures increases. When the identical roughness height is imposed, the scales of the u'-structure are generally large for the 2D rod rough-wall compared to that for the 3D cuboid rough-wall. Although not shown here, the population trends of the u'-streaks exhibit that large populations of wider and longer coherent structures as the roughness height increases for the 2D and 3D rough-walls attribute to the formation of the spatial correlation contours (Lee et al. 2016).

However, there remains a question of how long structures are frequently created over rough-walls. The time evolution of the instantaneous flow fields are explored in detail to address this question concerning to the streamwise scale growth for the flows over the rough-walls. The main idea is that

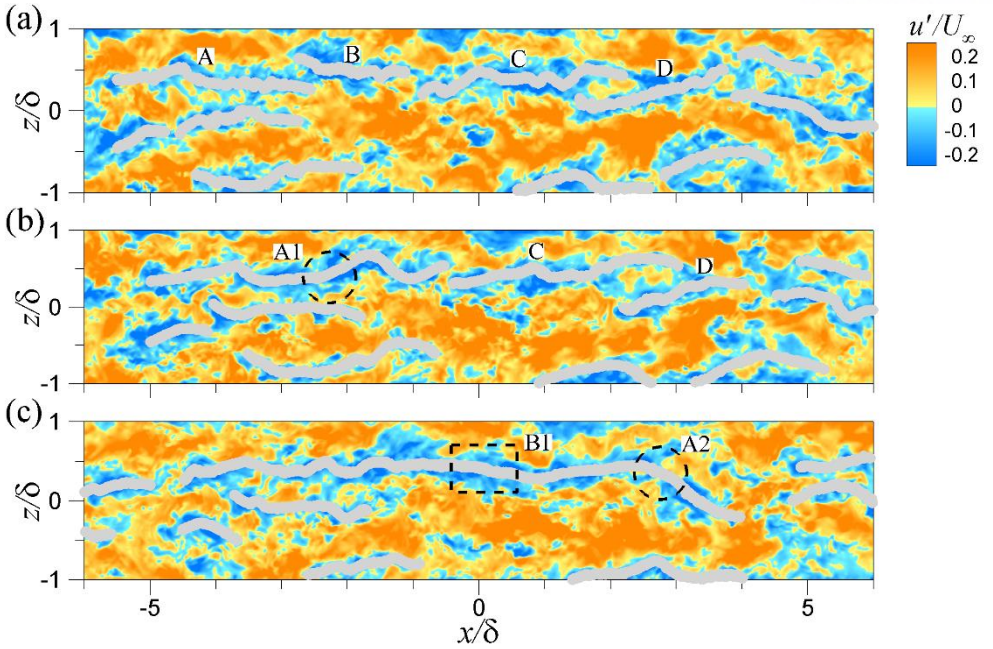

Figure 15 Time evolution of the instantaneous flow fields for the δ-scaled u'-structures for 2DK15 on the xz-plane at $y'/\delta = 0.2$: (a) $t = t_{ref} - 2\Delta t$, (b) $t = t_{ref} - \Delta t$ and (c) $t = t_{ref}$. Here, the time interval is $\Delta t U_\infty/\theta_{in} = 32$. The labels 'A', 'B', 'C' and 'D' indicate the large-scale u'-structures (~2-3δ). The label 'A1' with a dashed circle indicates a spanwise merged u'-structure between 'A' and 'B'. The label 'B1' with a dashed rectangle indicates a streamwise merged u'-structure between 'A1' and 'C'. The label 'A2' with a dashed circle indicates a spanwise merged u'-structure between 'C' and 'D'. Grey lines indicate negative characteristic lines.

small scales organize coherently to create larger scales, as suggested by the previous studies (Kim & Adrian 1999; Tomkins & Adrian 2003). In order to present how a very long u'-streaks is generated, the time-evolving instantaneous flow field is shown. Only the 2D rod roughened-wall with $k/\theta_{in} = 1.5$ is plotted as a representative case (shown in figure 12b), and an identical process is found for the smooth- and the 3D cuboid-roughened walls. At $t = t_{ref} - 2\Delta t$ in figure 15(a), there are four adjacent streaks (labeled as A, B, C and D) located at $-5 < x/\delta < 5$ and $0 < z/\delta < 1$ with streamwise extents of approximately 2-3δ (i.e., LSMs). For the 'A' and 'B' structures, the downstream and upstream portions of the negative structures are overlapped in the downstream direction, although there is spanwise separation between them. These two structures evolve slowly over time, moving with similar convection velocities along the streamwise direction, and there occurs significant spanwise interaction between them, resulting in a streamwise-aligned longer negative u'-structure (A1) with a length of 5δ. In addition to the spanwise merging event at $x/\delta = -2.5$, an another spanwise merging event (marked 'A2') between the 'C' and 'D' structures located at $0 < x/\delta < 4$ is observed, indicating the persistence of the spanwise merging event between the LSMs to increase the streamwise scale of the structure.

It is should be noted that the spanwise merging process should not be confused with the streamwise concatenation process between LSMs in wall-bounded turbulent flows, which also creates longer sequences of VLSMs (Lee & Sung 2011; Lee et al. 2014; Lee et al. 2019). An example of a streamwise merging event between LSMs is shown in figure 15, as highlighted by the dashed rectangle (denoted by 'B1'). For the streamwise concatenation process, two adjacent LSMs (i.e., 'B' and 'C') are proximal in the downstream direction (without an overlapped region in the spanwise direction) to form a merging event due to the different convection velocities between the 'B' and 'C' structures (Lee et al. 2014). Although a detailed description of the streamwise merging process to form a VLSM is not given here for simplicity, the overall process as observed in the present study is very similar to that from our previous studies in smooth-wall TBL and channel/pipe flows (Lee & Sung 2011; Lee et al. 2014; Lee et al. 2019). The streamwise concatenation process is associated with two kinematics of the stretching and shearing of LSMs (Lee et al. 2019), whereas the spanwise merging between LSMs is mainly a simple piecing together (although interactions between the inner vortices of the merging LSMs may, and most likely do occur.). Lee et al. (2016) reported that as the spanwise interaction of LSMs occurs at a streamwise position, the inner vortices with opposite swirls based on the hairpin vortex model are annihilated, with only the larger outer vortices eventually surviving (Tomkins & Adrian 2003). As described above, the spanwise length scale of structures over rough-walls increases with an increase of the roughness height due to large-scale turbulent motions generated by infinite (or finite) widths of the present roughness (Volino et al. 2009), and the increased width of the structures can lead to frequent spanwise merging between the LSMs to form VLSMs. Although spanwise merging events occur frequently between adjacent LSMs, this process is also expected to occur between small-scale motions. However, because the spanwise length scale of the small-scale motions is relatively small, the spanwise merging between LSMs is the primary contributor of the formation of VLSMs.

In order to evaluate the frequency of spanwise merging events with an increase of the roughness height for the 2D rod and 3D cuboid in a statistical sense, the streak-merging events are counted using instantaneous snapshots. The inset in figure 16 shows a schematic to explain the streak-merging detection method. Because the merging event is central when describing the time-dependent scale change, we initially identify significant streamwise scale growth with an interval of Δt_{track}. When scale growth at the present time step (t_{ref}) is observed regardless of the merging type, the streaks at the previous time step ($t_{ref} - \Delta t_{track}$) are traced to determine if the event between LSMs is created by the streamwise or spanwise merging process. By tracking all streaks at each snapshot, the spanwise merging events for smooth and rough-walls with an increase of the roughness height are estimated. Figure 16 shows the variation of the streak-merging frequency (ρ_m) with respect to the value of k/δ. Here, ρ_m is defined as the average number of streak spanwise merging events per unit of span. It is clear that the LSMs tend to merge in the spanwise direction to form VLSMs as the value of k/δ increases, consistent with our observation from the instantaneous analysis. It should be noted that although the streak-

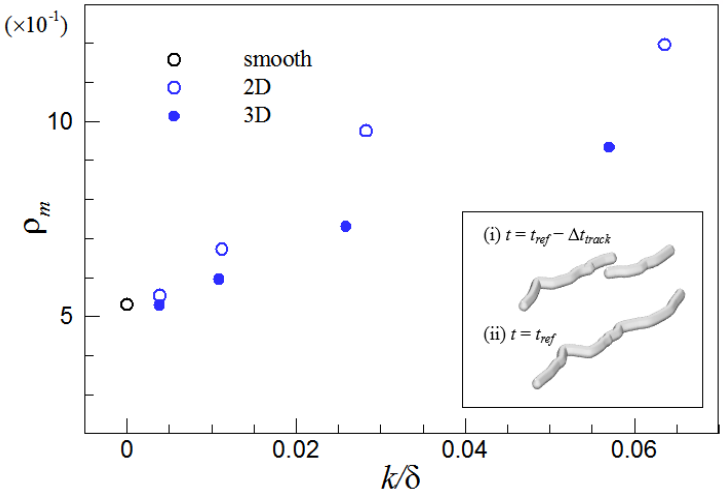

Figure 16 Variations of the streak-merging frequency (ρ_m) at y'/δ = 0.2 with an increase of k/δ. In the inset, schematic of the streak-merging process on the *xz*-plane is shown. Here, the time interval is $\Delta t_{track} U_\infty/\theta_{in}$ = 32.

merging frequency increases slightly with an increase of the boundary layer thickness along the streamwise direction for each case, the trend of the streak-merging frequency in variation with respect to the roughness height was not changed significantly. In addition, the frequency of the occurrence of streamwise merging events was not sensitive to the variation of the roughness height, implying that the streamwise concatenation process is not affected by the surface roughness.

The wavering feature of the characteristic line is identified using a similar approach devised by Kevin et al. (2019) in figure 17. In a DNS study of the turbulent pipe flow over a smooth-wall, Baltzer et al. (2013) reported that apparent meandering of VLSM is induced as a consequence of spanwise-offset LSMs when the LSMs are merged by a streamwise concatenation process. If a VLSM is created due to the spanwise merging as described above, the wavering will also be enhanced by the spanwise-offset LSMs in rough-wall TBL flows. In order to estimate the wavering (or meandering) feature, we quantify the 'waviness' of the characteristic lines and employ it as a metric (Kevin et al. 2019). The instantaneous flow field (shown in figure 12a) of the δ-scaled u'-structures on the *xz*-plane in a smooth-wall TBL flow is shown in figure 17(a). In the figure, the black dashed line plotted over each characteristic line indicates the corresponding linear fit according to the least-squares method. Accordingly, we treat these lines as projected fluctuation signals $\tilde{z}$ about the fitted line (see the inset in figure 17a with the coordinate system) and compute the root mean square of these signals. Here, only long characteristic lines ($\geq 1\delta$) are utilized for the measurement because LSMs are found to scale on the boundary layer thickness with average dimensions greater 1δ (Wu et al. 2012). In figure 17(b), it is clear that the meandering behavior ($\tilde{z}_{rms}$) of the negative u'-structures increases with an increase of k/δ for the

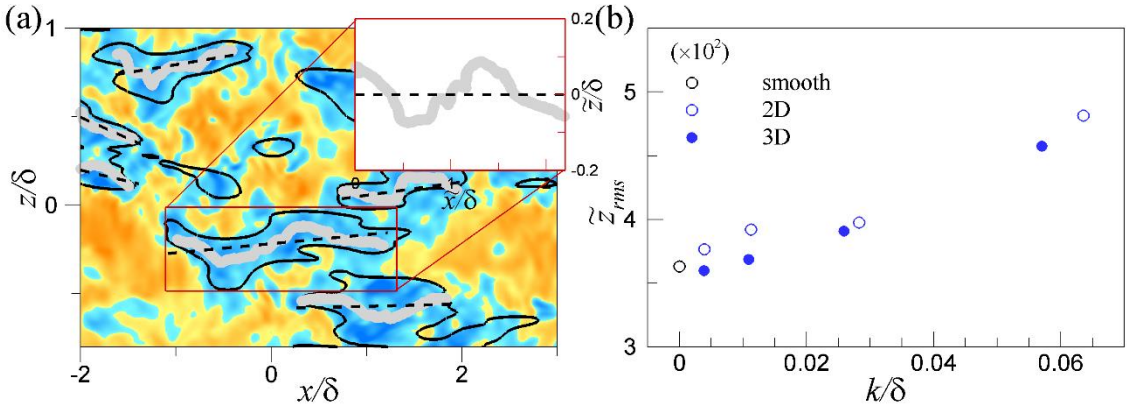

Figure 17 (a) Instantaneous flow field of the δ-scaled u'-structures on the xz-plane in the smooth-wall TBL flow and (b) the root mean square ($\tilde{z}_{rms}$) of the meandering motion with an increase of k/δ at y'/δ = 0.2. In (a), dashed lines indicate the linear fit of each characteristic line. In the inset, $\tilde{x}$ and $\tilde{z}$ are correspondingly the projected linear fits of a characteristic line to the streamwise and spanwise directions.

2D and 3D roughness cases. These results indicate that the large-scale turbulence becomes increasingly wavy with an increase of k/δ due to the active spanwise merging events between the spanwise-offset LSMs. The increased meandering magnitude for the 2D rod roughness compared to the 3D cuboid roughness is mostly attributed to the infinite width of the surface roughness.

5. Summary and conclusion

In the present study, we undertook DNSs of spatially developing TBLs over 2D rod-roughened walls and 3D cuboid-roughened walls to investigate the effects of the roughness height ($13 \leq \delta/k \leq 250$) on the turbulence statistics and coherent structures. Our inspection of the flow parameters of the skin frictional drag, form drag, friction velocity and virtual origin showed that these quantities are strongly dependent on k/θ_{in}. Compared to the smooth-wall case, the growth rates of the boundary layer parameters (i.e., δ, δ^* and θ) increased, and the 2D rod cases showed greater effects on the flows compared to those in the 3D cuboid cases for all values of k/θ_{in}. As the impact of the surface roughness increased with an increase of k/θ_{in}, the downstream distance required for a new equilibrium state increased due to the relatively strong flow disturbance near the step change. The roughness function (ΔU^+) extracted from the mean velocity profiles in the equilibrium state increased continuously with an increase of k/θ_{in} for the 2D rod and 3D cuboid roughness, with similar behavior observed in the magnitude of the Reynolds stresses in the outer region. For square-edged roughness, wall-similarity in the outer layer was achieved when the roughness type was classified into the hydraulically smooth regime, and the critical roughness height for outer layer wall-similarity compared to the boundary layer thickness was $\delta/k = 250$ for the 2D rod and $\delta/k = 100$ for the 3D cuboid. To predict the occurrence of outer layer similarity, the roughness function ($\Delta U^+ \leq 1.2$) was parameterized by k_s^+ ($k_s^+ \leq 11$) and v_w^+ ($v_w^+ \leq 0.11$) by simple corresponding relationships. Contrary to previous observations in which the tendency of the wall-friction parameters differs from that of the Reynolds stresses in the outer layer when varying the streamwise and spanwise pitches between the roughness elements (Lee et al. 2012; Ahn et al. 2013), our results showed that the variations of the wall-friction parameters and the outer layer Reynolds stresses are similar with an increase of the roughness height, suggesting a strong influence of the roughness height on both the near-wall region and in the outer region. The increase of the Reynolds stresses in the outer layer with an increase of the roughness height was explained by a large population of long u'-structures with high energy over rough-wall flows. Because the spanwise length scale of structures over the rough-walls increased continuously with an increase of the roughness height for the 2D and 3D roughness cases, the increased width of the u'-structures led to frequent spanwise merging events between adjacent LSMs to form VLSMs. The active spanwise merging events between the spanwise-offset LSMs increased the appearance of meandering significantly as the value of k/δ increased. Finally, we emphasize that the results in the present study might be affected by roughness type and array, e.g., 3D roughness with a large variety of roughness sizes, and hence numerical and experimental studies in future might be able to assess a critical roughness height for the outer layer similarity more clearly.

References

1. Adrian, R. J., Meinhart, C. D., & Tomkins, C. D. (2000). Vortex organization in the outer region of the turbulent boundary layer. *Journal of fluid Mechanics*, *422*, 1-54.
2. Ahn, J., Lee, J. H., & Sung, H. J. (2013). Statistics of the turbulent boundary layers over 3D cube-roughened walls. *International journal of heat and fluid flow*, *44*, 394-402.
3. Akinlade, O. G., Bergstrom, D. J., Tachie, M. F., & Castillo, L. (2004). Outer flow scaling of smooth and rough wall turbulent boundary layers. *Experiments in Fluids*, *37*(4), 604-612.
4. Antonia, R. A., & Luxton, R. E. (1971). The response of a turbulent boundary layer to a step change in surface roughness Part 1. Smooth to rough. *Journal of Fluid Mechanics*, *48*(4), 721-761.
5. Baltzer, J. R., Adrian, R. J., & Wu, X. (2013). Structural organization of large and very large scales in turbulent pipe flow simulation. *Journal of Fluid Mechanics*, *720*, 236.
6. Bandyopadhyay, P. R. (1987). Rough-wall turbulent boundary layers in the transition regime. *Journal of Fluid Mechanics*, *180*, 231-266.
7. Basley, J., Perret, L., & Mathis, R. (2019). Structure of high Reynolds number boundary layers over cube canopies. *Journal of Fluid Mechanics*, *870*, 460-491.
8. Bhaganagar, K., Kim, J., & Coleman, G. (2004). Effect of roughness on wall-bounded turbulence. *Flow, turbulence and combustion*, *72*(2-4), 463-492.
9. Burattini, P., Leonardi, S., Orlandi, P., & Antonia, R. A. (2008). Comparison between experiments and direct numerical simulations in a channel flow with roughness on one wall. *Journal of Fluid Mechanics*, *600*, 403.
10. Cheng, H., & Castro, I. P. (2002a). Near-wall flow development after a step change in surface roughness. *Boundary-Layer Meteorology*, *105*(3), 411-432.
11. Cheng, H., & Castro, I. P. (2002b). Near wall flow over urban-like roughness. *Boundary-Layer Meteorology*, *104*(2), 229-259.
12. Christensen, K. T., & Adrian, R. J. (2001). Statistical evidence of hairpin vortex packets in wall turbulence. *Journal of Fluid Mechanics*, *431*, 433.
13. Coceal, O., Dobre, A., Thomas, T. G., & Belcher, S. E. (2007). Structure of turbulent flow over regular arrays of cubical roughness. *Journal of Fluid Mechanics*, *589*, 375-409.
14. Colebrook, C. F., Blench, T., Chatley, H., Essex, E. H., Finniecome, J. R., Lacey, G., ... & Macdonald, G. G. (1939). Correspondence. turbulent flow in pipes, with particular reference to the transition region between the smooth and rough pipe laws.(includes plates). *Journal of the Institution of Civil engineers*, *12*(8), 393-422.
15. Efros, V., & Krogstad, P. Å. (2011). Development of a turbulent boundary layer after a step from smooth to rough surface. *Experiments in fluids*, *51*(6), 1563-1575.
16. Flack, K. A., Schultz, M. P., & Shapiro, T. A. (2005). Experimental support for Townsend's Reynolds number similarity hypothesis on rough walls. *Physics of Fluids*, *17*(3), 035102.
17. Flack, K. A., Schultz, M. P., & Connelly, J. S. (2007). Examination of a critical roughness height for outer layer similarity. *Physics of Fluids*, *19*(9), 095104.
18. Flack, K. A., & Schultz, M. P. (2014). Roughness effects on wall-bounded turbulent flows. *Physics of Fluids*, *26*(10), 101305.
19. Ganapathisubramani, B., Longmire, E. K., & Marusic, I. (2003). Characteristics of vortex packets

in turbulent boundary layers.

20. Hama, F. R. (1954). Boundary layer characteristics for smooth and rough surfaces. *Trans. Soc. Nav. Arch. Marine Engrs.*, *62*, 333-358.
21. Head, M. R., & Bandyopadhyay, P. (1981). New aspects of turbulent boundary-layer structure. *Journal of fluid mechanics*, *107*, 297-338.
22. Hutchins, N., & Marusic, I. (2007). Evidence of very long meandering features in the logarithmic region of turbulent boundary layers.
23. Jackson, P. S. (1981). On the displacement height in the logarithmic velocity profile. *Journal of fluid mechanics*, *111*, 15-25. Jackson, P. S. 1981 On the displacement height in the logarithmic velocity profile. *J. Fluid Mech.* **111**, 15-25.
24. Jiménez, J. (2004). Turbulent flows over rough walls. *Annu. Rev. Fluid Mech.*, *36*, 173-196.
25. Kevin, K., Monty, J., & Hutchins, N. (2019). The meandering behaviour of large-scale structures in turbulent boundary layers. *Journal of Fluid Mechanics*, *865*.
26. Kim, K. C., & Adrian, R. J. (1999). Very large-scale motion in the outer layer. *Physics of Fluids*, *11*(2), 417-422.
27. Kim, J., Kim, D., & Choi, H. (2001). An immersed-boundary finite-volume method for simulations of flow in complex geometries. *Journal of computational physics*, *171*(1), 132-150.
28. Kim, K., Baek, S. J., & Sung, H. J. (2002). An implicit velocity decoupling procedure for the incompressible Navier–Stokes equations. *International journal for numerical methods in fluids*, *38*(2), 125-138.
29. Krogstad, P. Å., & Antonia, R. A. (1999). Surface roughness effects in turbulent boundary layers. *Experiments in fluids*, *27*(5), 450-460.
30. Krogstad, P. Å., & Efros, V. (2012). About turbulence statistics in the outer part of a boundary layer developing over two-dimensional surface roughness. *Physics of Fluids*, *24*(7), 075112.
31. Krogstad, P. A., & Nickels, T. B. (2006). Turbulent boundary layer with a step change in surface roughness. In *Proceedings of CMFF'06: Conference on Modelling Fluid Flow-13th Event of the International Conference Series in Fluid Flow Technologies v. 1* (Vol. 1, pp. 568-573). CMFF.
32. Lee, J., Lee, J. H., Choi, J. I., & Sung, H. J. (2014). Spatial organization of large-and very-large-scale motions in a turbulent channel flow. *Journal of fluid mechanics*, *749*, 818-840.
33. Lee, J., Kim, J. H., & Lee, J. H. (2016). Scale growth of structures in the turbulent boundary layer with a rod-roughened wall. *Physics of Fluids*, *28*(1), 015104.
34. Lee, J. H., Lee, S. H., Kim, K., & Sung, H. J. (2009). Structure of the turbulent boundary layer over a rod-roughened wall. *International journal of heat and fluid flow*, *30*(6), 1087-1098.
35. Lee, J. H., Sung, H. J., & Krogstad, P. Å. (2011). Direct numerical simulation of the turbulent boundary layer over a cube-roughened wall. *Journal of Fluid Mechanics*, *669*, 397.
36. Lee, J. H., & Sung, H. J. (2011). Very-large-scale motions in a turbulent boundary layer. *Journal of Fluid Mechanics*, *673*, 80.
37. Lee, J. H., Seena, A., Lee, S. H., & Sung, H. J. (2012). Turbulent boundary layers over rod-and cube-roughened walls. *Journal of Turbulence*, *13*(1), N40.
38. Lee, J. H., Sung, H. J., & Adrian, R. J. (2019). Space–time formation of very-large-scale motions in turbulent pipe flow. *Journal of Fluid Mechanics*, *881*, 1010-1047.
39. Lee, S. H., & Sung, H. J. (2007). Direct numerical simulation of the turbulent boundary layer over a rod-roughened wall. *Journal of Fluid Mechanics*, *584*, 125-146.

40. Leonardi, S., Orlandi, P., Smalley, R. J., Djenidi, L., & Antonia, R. A. (2003). Direct numerical simulations of turbulent channel flow with transverse square bars on one wall. *Journal of Fluid Mechanics*, *491*, 229.
41. Leonardi, S., & Castro, I. P. (2010). Channel flow over large cube roughness: a direct numerical simulation study. *Journal of Fluid Mechanics*, *651*, 519-539.
42. Ligrani, P. M., & Moffat, R. J. (1986). Structure of transitionally rough and fully rough turbulent boundary layers. *Journal of Fluid Mechanics*, *162*, 69-98.
43. Lu, S. S., & Willmarth, W. W. (1973). Measurements of the structure of the Reynolds stress in a turbulent boundary layer. *Journal of Fluid Mechanics*, *60*(3), 481-511.
44. Lund, T. S., Wu, X., & Squires, K. D. (1998). Generation of turbulent inflow data for spatially-developing boundary layer simulations. *Journal of computational physics*, *140*(2), 233-258.
45. Mejia-Alvarez, R., Wu, Y., & Christensen, K. T. (2014). Observations of meandering superstructures in the roughness sublayer of a turbulent boundary layer. *International journal of heat and fluid flow*, *48*, 43-51.
46. Nadeem, M., Lee, J. H., Lee, J., & Sung, H. J. (2015). Turbulent boundary layers over sparsely-spaced rod-roughened walls. *International Journal of Heat and Fluid Flow*, *56*, 16-27.
47. Nikuradse, J. (1933). Laws of flow in rough pipes, Technial memorandum 1292. *National Advisory Comitee for Aeronautics, Washington, DC*.
48. Orlandi, P., Leonardi, S., & Antonia, R. A. (2006). Turbulent channel flow with either transverse or longitudinal roughness elements on one wall. *Journal of Fluid Mechanics*, *561*, 279.
49. Orlandi, P., & Leonardi, S. (2008). Direct numerical simulation of three-dimensional turbulent rough channels: parameterization and flow physics. *Journal of Fluid Mechanics*, *606*, 399.
50. Placidi, M., & Ganapathisubramani, B. (2018). Turbulent flow over large roughness elements: effect of frontal and plan solidity on turbulence statistics and structure. *Boundary-layer meteorology*, *167*(1), 99-121.
51. Raupach, M. R., Antonia, R. A., & Rajagopalan, S. (1991). Rough-wall turbulent boundary layers.
52. Reynolds, R. T., & Castro, I. P. (2008). Measurements in an urban-type boundary layer. *Experiments in Fluids*, *45*(1), 141-156.
53. Schlichting, H. (1937). *Experimental investigation of the problem of surface roughness* (No. 823). National Advisory Commitee for Aeronautics.
54. Schlichting, H. (1987). Boundary Layer Theory, reissue of 7th Edn.
55. Schultz, M. P., & Flack, K. A. (2005). Outer layer similarity in fully rough turbulent boundary layers. *Experiments in fluids*, *38*(3), 328-340.
56. Schultz, M. P., & Flack, K. A. (2007). The rough-wall turbulent boundary layer from the hydraulically smooth to the fully rough regime. *Journal of Fluid Mechanics*, *580*, 381.
57. Schultz, M. P., & Flack, K. A. (2009). Turbulent boundary layers on a systematically varied rough wall. *Physics of Fluids*, *21*(1), 015104.
58. Shockling, M. A., Allen, J. J., & Smits, A. J. (2006). Roughness effects in turbulent pipe flow. *Journal of Fluid Mechanics*, *564*, 267.
59. Smalley, R. J., Antonia, R. A., & Djenidi, L. (2001). Self-preservation of rough-wall turbulent boundary layers. *European Journal of Mechanics-B/Fluids*, *20*(5), 591-602.
60. Spalart, P. R. (1988). Direct simulation of a turbulent boundary layer up to R θ= 1410. *Journal of fluid mechanics*, *187*, 61-98.

61. Squire, D. T., Morrill-Winter, C., Hutchins, N., Schultz, M. P., Klewicki, J. C., & Marusic, I. (2016). Comparison of turbulent boundary layers over smooth and rough surfaces up to high Reynolds numbers. *Journal of Fluid Mechanics*, *795*, 210.
62. Squire, D. T., Hutchins, N., Morrill-Winter, C., Schultz, M. P., Klewicki, J. C., & Marusic, I. (2017). Applicability of Taylor's hypothesis in rough-and smooth-wall boundary layers. *Journal of Fluid Mechanics*, *812*, 398-417.
63. Tomkins, C. D., & Adrian, R. J. (2002). *Spanwise structure and scale growth in turbulent boundary layers*. Department of Theoretical and Applied Mechanics (UIUC).
64. Townsend, A. A. R. (1980). *The structure of turbulent shear flow*. Cambridge university press.
65. Volino, R. J., Schultz, M. P., & Flack, K. A. (2007). Turbulence structure in rough-and smooth-wall boundary layers. *Journal of Fluid Mechanics*, *592*, 263-293.
66. Volino, R. J., Schultz, M. P., & Flack, K. A. (2009). Turbulence structure in a boundary layer with two-dimensional roughness. *Journal of Fluid Mechanics*, *635*, 75-101.
67. Volino, R. J., Schultz, M. P., & Flack, K. A. (2011). Turbulence structure in boundary layers over periodic two-and three-dimensional roughness. *Journal of Fluid Mechanics*, *676*, 172.
68. Wu, Y., & Christensen, K. T. (2007). Outer-layer similarity in the presence of a practical rough-wall topography. *Physics of Fluids*, *19*(8), 085108.
69. Wu, Y., & Christensen, K. T. (2010). Spatial structure of a turbulent boundary layer with irregular surface roughness. *Journal of Fluid Mechanics*, *655*, 380.
70. Wu, X., Baltzer, J. R., & Adrian, R. J. (2012). Direct numerical simulation of a 30R long turbulent pipe flow at R+= 685: large-and very large-scale motions. *Journal of Fluid Mechanics*, *698*, 235.

Acknowledgement

I would like to express my deep gratitude to all who supported my work and contributed to this master thesis.

Firstly, the deepest appreciation goes to my advisor Prof. Jae Hwa Lee for the motivation, encouragement and guidance in all the time of research and writing of the thesis. I am deeply grateful to the thesis committee: Prof. Chun Sang Yoo and Prof. Jooha Kim for offering insightful and valuable comments and constructive criticisms.

I would like to extend my gratitude to all the member of FPCL Lab members including the graduated senior, Young Mo Lee, Young Dal Jeong, Min Je Kim, Hyeung Jae Lim, Hyeon Gyu Hwang, Jun Hyuk Hwang, Chang Geol Lee, Sun Youb Lee, Jeong Hyun Kim and Ki Ho Ahn for their warm help during my master's course. Special appreciation is given to Young Mo Lee who had deeply assisted me throughout the research. Owing to the assistance of all the lab members, I was able to have a great time during the master's course

I would like to express my heartfelt gratitude to my parents, Eek Ki Choi and Jeong Hyun Na, and my brother, Jun Hyun Choi, for continuous love and support throughout my graduate school life.

I am very thankful for my friends, Yun Jae Hwang, Ji Heon Kim, Ji Hye Kim, Su Bin Seo, Seo Jin Kim, Yu Ri Jang and Da Som Hwang who have always believed and supported me and my work.